AUTHOR: W. H. Kyong

TITLE OF THESIS: A Numerical Description for Spherical Imploding

Shock Waves

DEPARTMENT: Mechanical Engineering

DEGREE: Master of Engineering

SUMMARY

To develop an accurate and time-saving numerical scheme for imploding shock waves, the methods of characteristics, both of standard scheme and Hartree's scheme, and the method of finite difference are applied for the energy-driven shock model. The starting conditions for numerical calculations are determined from exact analytical third-order solutions.

The results clearly show that Hartree's scheme is very accurate, and the analytical solutions are excellent for determining the starting conditions.

Close study of the local energy distribution, singularity, similarity, limiting characteristic and geometrical effects clearly exhibits the emergence of the self-amplifying mechanism, the property of "forgetfulness" and the existence of the self-similar solution.

A NUMERICAL DESCRIPTION FOR SPHERICAL IMPLODING SHOCK WAVES

bу

W. H. Kyong

A thesis submitted to the Faculty of Graduate Studies
and Research in partial fulfillment of the
requirements for the degree of
Master of Engineering

Department of Mechanical Engineering
McGill University
Montreal, Canada

TABLE OF CONTENTS

				PAGE
TABLE OF	? CON	TENTS	•	
NOME NCL	ATURE		. -	
LIST OF	FIGU	RES A	ND TABLE	
ABS TRACT	ľ			1
ACKNOWLE	EDGEM	ENTS		3
CHAPTER	I	INTR	ODUCTION	4
		1.1	Historical Statement of Previous Work	4
		1.2	The Motivation of Selecting the	
			Numerical Schemes	7
		1.3	The Outline of the Present Work	9
CHAPTER	II	FORM	ULATION	12
		2.1	Model, Basic Equations and Boundary Conditions	12
		2.2	Initial Starting Data	15
		2.3	Characteristic Equations	21
CHAPTER	HAPTER III NUMERICAL ANALYSIS		RICAL ANALYSIS	26
		3.1	Hartree's Constant Time Line Scheme	30
		3.2	Standard Characteristic Method	36
		3.3	Similarity Conditions	37
		3.4	Singularity Analysis	40
CHAPTER	IV	RESU	LTS AND DISCUSSION	45
		4.1	On the Numerical Schemes	45

				PAGE
		4.2	Numerical Solutions	. 49
		4.3	Self-Amplifying Mechanism, Initial Condition	
			Forgetfulness and Self-Similarity	51
		4.4	Geometrical Effects	54
ι	REFERENCES			58
	FIGURES			
	TA DI E			

•

•

NOMENCLATURE

Symbol	<u>Definition</u>
a, b	Coefficients of quadratic interpolation (Eq. 3.9)
A, A', A"	Dimensional constant of the shock trajectory with
	respect to time t, t' and ? , respectively
С	Speed of sound
c'	Non-dimensional speed of sound
c ⁺ , c ⁻ , c ^o	Physical characteristics, positive, negative and of
	particle path
c* j	Energy reduced speed of sound of initial condition
-	(Eq. 2.22)
e	Internal energy per unit mass
Eo	Total initiation energy released instantaneously
Es.D.	Shock surface energy density ratio (Eq. 4.1)
Ev.D.	Volumetric energy density ratio of the shocked gas
	(Eq. 4.2)
Ev.D.s	Volumetric energy density ratio on the shock surface
	(Eq. 4.3)
f	Non-dimensional pressure (Eq. 2.14)
f ⁽ⁿ⁾	Nth order perturbation coefficient of f (Eq. 2.25)

Symbol **Definition** Fn Nth order perturbation coefficient of shock velocity (Eq. 2.26) G Arbitrary function to be interpolated quadratically Integral of internal energy (Eq. 2.24) I Numerical constant (P.P. 15) j Numerical constant (Eq. 2.20) k i M_s Shock Mach number N Time exponent of the shock trajectory Pressure р p' Non-dimensional pressure (Eq. 2.33) Space coordinate r r' Non-dimensional space coordinate (Eq. 2.28) Space coordinate of back boundary r r'h Non-dimensional space coordinate of back boundary R Radius of spherical wall R Instantaneous shock radius Rs, Rs First and second derivative of $R_{_{\mathbf{S}}}$ with respect to time t R's Non-dimensional shock radius (Eq. 2.29)

Symbol Definition R'_s(१) First derivative of R_s^{\dagger} with respect to time 2 So Spherical surface of the wall Instantaneous shock surface t Time t' Non-dimensional time (Eq. 3.11) Total time of collapse Energy reduced time (Eq. 2.20) Particle velocity u' Non-dimensional particle velocity Volume Non-dimensional shock radius (Eq. 2.11) xs x, x, First and second derivative of \mathbf{x}_{s} with respect to time t **x**_s(?) First derivative of x_s with respect to time γ Shock distance (Eq. 2.10) X Ϋ́ς First derivative of X_{s} with respect to time t Ratio of specific heats 8 Shock decay coefficient (Eq. 2.18) θ $\theta_{\mathbf{R_s}}$ Shock decay coefficient (Eq. 3.12)

Symbol	<u>Definition</u>
$\theta_{\mathbf{x_s}}$	Shock decay coefficient (Eq. 3.13)
5	Non-dimensional space coordinate (Eq. 2.9)
5 s	Non-dimensional similarity space coordinate (P.P. 37)
6	Density
e'	Non-dimensional density (Eq. 2.31)
Ψ	Non-dimensional density (Eq. 2.12)
ψ ⁽ⁿ⁾	Nth order perturbation coefficient of ψ (Eq. 2.25)
φ	Non-dimensional particle velocity (Eq. 2.13)
φ ⁽ⁿ⁾	Nth order perturbation coefficient of ϕ (Eq. 2.25)
?	Non-dimensional time (Eq. 2.19)
$7_{\rm c}$	Total time of collapse (Eq. 3.11)
3	Total energy density (Eq. 3.30)
87	Thermal pressure energy density (Eq. 3.30)
Eĸ	Kinetic energy density (Eq. 3.30)
Subscripts	
() _o	Undisturbed conditions
() _s	Conditions immediately behind the shock front
()'	Non-dimensional variables for the method of character-
	istics

LIST OF FIGURES AND TABLE

Figure

- Shock Trajectory and Velocity vs Shock Radius for $c_{j}^{*2} = 0$, j = 2, $\gamma = 1.4$
- 2 Profiles of Density, Particle Velocity and Pressure on the Shock Front for $c_{j}^{*2} = 0$, .05, .1
- Pressure Profiles for $c_{i}^{*2} = 0$
- 4 Particle Velocity Profiles for $c_j^{*2} = 0$
- Density Profiles for $c_j^{*2} = 0$
- 6 Local Energy Density Distributions for $c_{j}^{*2} = 0$
- 7 Limiting Characteristic, Singularity and Similarity

 Lines for $c_{j}^{*2} = 0$
- 8 Energy Density Peak and Energy Density Profiles on the Shock Front and on the Singularity Line
- 9 Density and Pressure Peaks for $c_{j}^{*2} = 0$, .05, .1
- 10 Asymptotic Nature of Shock Pressure and Shock Mach Number for $c_j^{*2} = 0$, .05, .1
- Shock Trajectories and Characteristic Points for $c_{j}^{*2} = 0$, .01, .05, .1
- 12 Shock Velocities vs Shock Radius for $c_{j}^{*2} = 0$, .01, .1

Figure

- Shock Trajectories and Shock Wave Velocities for Different Starting Time Lines, $c_{j}^{*2} = 1.0$, Hartree Scheme
- Density, Pressure and Particle Velocity Profiles for Different Starting Time Lines, $c_{j}^{*2} = 1.0$, Hartree Scheme
- Shock Trajectories and Shock Wave Velocities for Different Starting Time Lines, $c_j^{*2}=0$, Standard Scheme
- 16 Characteristic Lines and Back Boundary
- 17 Geometrical Effects

TABLE

1 Variation of A, N and t_c with $c_j^{*2} = 0$, .005, .01

ABSTRACT

It is the aim of the present work first, to develop a numerical scheme which is both accurate and time-saving in achieving an exact solution for imploding shock waves and second, to investigate the peculiar property of "forgetfulness" exhibited by collapsing shock waves, a property which leads to self-propagation of such waves. This self-propagating mechanism for converging shock waves is apparent in the existence of the limiting self-similar solution which is independent of initial conditions.

The theoretical model chosen in this work is that of a collapsing shock wave generated instantaneously by an impulsive release of energy at some finite initial radius. The governing equations of motion together with the appropriate boundary conditions are then integrated numerically using the method of characteristics both in the conventional manner and with Hartree's constant time line scheme. A set of exact numerical solutions is thereby achieved for the entire range of collapse of such a shock wave.

Through recent work on analytical description for the initial phases of collapse on the same model, Bach and Lee (1967) provided an excellent method for determining the starting conditions for numerical calculations. The third order solutions were found to be extremely good for the early stage of strong initiation. Hence, the initial starting data on the first time line, which usually is one of the

difficulties to carry on numerical calculation with this model, were calculated in the present work from this third order solution. In this manner tremendous time-saving of the order of several minutes of computation time could be achieved for the whole range of collapse.

The results of the present work clearly show the very early development of the limiting characteristic, singularities, very narrow positive pressure gradient at the shock wave and surprisingly rapid correction of the error which imposed by the third order solution on the first time line in the weak initiation. The narrow positive pressure gradients at the shock wave suggest Hartree's scheme is more accurate and applicable in this case than the standard scheme. The rapid correction of the error of initial data indicates rapid "forgetfulness" in this early stage and so the third order solution provides excellent initial data even for weak initiation.

Close study of the local energy distributions and of the energy gradients on the shock front, singularity line and limiting characteristic line clearly exhibit the emergence of the self-amplifying mechanism and the property of "forgetfulness" of initial conditions for converging shock waves. The solutions, in fact, recover the power law exponent for the shock trajectory as obtained in Guderley's limiting similarity solution.

ACKNOWLEDGEMENTS

The Author would like to express his gratitude to Professors G. G. Bach and J. H. S. Lee for suggesting the problem and for the guidance and encouragement generously given throughout the course of the work.

The Author also wishes to thank Professor J. H. T. Wu for his continuous encouragement and support.

Special thanks are due to Dr. R. Knystautas for proofreading the paper and to Miss N. E. Boyce for typing the manuscript.

The support of the National Research Council of Canada under Grant No. A-118 of the work is gratefully acknowledged.

CHAPTER I

INTRODUCTION

1.1 Historical Statement of Previous Work

For a description of the motion of a converging cylindrical or spherical shock wave one may divide its whole range of collapse into three different regimes; namely, the early stage where approximate analytical solutions or sometimes planar strong blast wave solutions are applicable, the late stage in the vicinity of the center of convergence where a similarity solution exists and the intermediate stage of moderate shock strength.

It is well-known that a converging symmetrical shock wave in a compressible fluid becomes extremely strong as it converges towards the center and in theory can result in infinite pressure and temperature at the center. For this late stage, mainly due to the area diminishing effect, the shock becomes so strong that the counterpressure effect can be neglected and the so-called similarity solutions exist.

The first results for this late stage were given by Guderley (1942), Butler (1954) and Stanyukovich (1955), and the nature of the motion has already been extensively investigated. Through other problems having great similarity to that of converging shocks, for example, cavitation in water, climbing a bore on a beach, the existence of similarity solution has been discussed.

The similarity solution, however, cannot be applied for intermediate regions where the shock has moderate strength and characteristic length. Many non-similar techniques were developed and applied to solve for this region. Lee (1966) applied Oshima's quasi-similarity method, Sakurai's perturbation method and Porzel-Zaker's power law density method as in explosion problems, and Welsh (1966) perturbed the similarity solution obtaining first order corrections in inverse shock velocity squared. Both succeeded in accounting for non-similar effects due to finite shock strength, but the validity of their solutions is still very confined to the center of convergence.

Neglecting all the other effects but considering only area diminishing effect, Chester (1954)--Chisnell (1955)--Whitham (1958) extended the solution to account for non-similar effects without using the similarity solution and got fairly good results for the shock front properties. Although these approximate solutions determine the similarity exponent for the shock trajectory quite well, they cannot yield any estimate of fluid properties.

For the early stage, however, several approximate analytical solutions can be readily applied. In particular, Bach and Lee (1967) provided an accurate and complete description for the early stage of collapse. For strong initiation, the shock was shown to be similar to a strong planar blast wave. For finite energy initiation, the perturbation solution is an asymptotic series and diverges very rapidly. Thus the range of validity is extremely limited again and the existence of the asymptotic nature of the solution can be observed qualitatively.

Therefore, in general, similar or non-similar analytical solutions can describe the motion in part for extremely limited regions but can hardly give the solution for the whole range of collapse under arbitrary initial conditions. For a complete description of imploding shock waves, one has to resort to a numerical scheme exploiting the advantages of high speed electronic digital computers.

Payne (1957) was the first to attempt a numerical solution for cylindrical imploding shocks based on the diaphragm model of initiations using Lax's original finite difference method. His solution gives general features which resemble those of Guderley solutions but greatly underestimates the shock properties and the thermodynamic states of the flow field.

Lax's finite difference scheme introduces an artificial viscosity effect which tends to smooth out the shock discontinuity over several mesh points. It seems reasonable to state that the method cannot give suitable accuracy especially at the shock front, nor can it detect the extremely narrow pressure peak immediately behind the shock in the implosion problem. Moreover, the scheme is extremely time consuming, taking typically 16 hours for a calculation.

It seems that, up to the present, no complete numerical description has been given for this problem. Thus it is one of the fundamental motivations of this paper to develop a suitable numerical scheme which will cover the whole range of collapse with suitable accuracy and reasonable computer times.

On the other hand, the self-amplifying nature of imploding shock

waves was first observed experimentally by Kantrowitz (1953). Zeldovich and Rayzer (1965) have indicated that the form of limiting solution does not depend on the initial conditions nor on the initial shock generating mechanism, and there always occurs forgetfulness of initial conditions. It was also suggested that the limiting solution does not forget completely about the initial conditions, but selects the memory through A and keeps a constant value of N irrespective of initial conditions in the power law shock trajectory $R_s = A(t_s - t)^N$.

In many other problems of analogous nature to that of imploding shock motion, forgetfulness was also observed. For example, Meyer and Ho (1962), Keller, Levine and Whitham (1960) observed this effect in the problem of the climb of a bore onto a sloping beach, and Hunter (1960, 1963), Akinsete (1968) in the problem of collapse of spherical bubbles in water.

Then to what extent does a limiting solution forget the initial conditions, where and how does the self-amplifying mechanism start and finally emerge into a limiting self-similar solution? What is the overall picture of the imploding shock motion? An attempt to answer these questions constitutes another motivation of this paper.

1.2 The Motivation of Selecting the Numerical Schemes

Among the three numerical methods of solving the set of non-linear partial differential equations widely used in this field, namely, the method of finite differences, the method of characteristics and the method of integral relations, the first two of them were considered for this problem.

Selecting the scheme, in addition to easy control and time-saving, stability and starting data, particular attention was placed on the possibility of clear definition of the shock discontinuity due to the importance of determining the correct shock trajectory in the implosion problem.

As it is possible to impose exact shock relationships on the shock discontinuity in the finite difference method, if we use non-dimensionalized basic equations by specially defined variables as in Bach and Lee (1967), one may set up a suitable finite difference scheme which needs no artificial viscosity term. A set of calculations was carried out by applying a semi-implicit scheme with second order accuracy. However, the attempt was not successful due to the insensitivity of the energy integral, through which we can determine the shock decay coefficient θ (defined as Eq. 2.18) on each successive time step.

To avoid this difficulty of determining θ , one can drop out the parameter θ from the basic equations using original variables. Then it leads to introducing the artificial viscosity term in the method of finite differences which naturally results in a lack of accuracy. At the same time, it cannot give an exact treatment of the centered rarefaction wave nor of the contact surface in the propagation of converging shock waves generated by other means, such as the diaphragm which is seen in Payne's (1957) paper.

Meanwhile, the method of characteristics can assure the clear definition of the shock wave and is suitable to treat rarefaction waves and contact surfaces. It admits of considerable mathematical rigor

(uniqueness and convergence have been proved). Both numerical techniques using the method of characteristics with standard or constant time line schemes, were recently proven to be superior to the finite difference method with the artificial viscosity term by Chou (1965, 1966, 1967, 1968) in explosion problems. It was also shown that both schemes give the same order of accuracy and are very accurate provided the region with extremely high speed of sound is excluded. Thus, it is quite natural to expect that both of two methods will yield accurate results when applied to the implosion problems.

From calculations in this paper, however, it becomes apparent that the standard scheme of the method of characteristics considerably underestimates states at the shock front due to the difficulty of detecting the narrow positive pressure gradient in the implosion problem, which is quite the opposite to the situation in the explosion problem.

1.3 The Outline of the Present Work

The initial starting data on the first time line are calculated following the analytical method of Bach and Lee (1967). The governing equations are then integrated numerically first by Hartree's constant time line scheme, second by the standard characteristic method on the model of the impulsively generated energy-driven shock.

The fluid properties on each time line including the shock trajectories are determined by Hartree's scheme setting the back boundary on $r/R_0 = 0.72 \, (R_s/R_0)$. Pressure and sound speed are interpolated quad-

ratically throughout the region, but the particle velocity is interpolated linearly.

To check the results on the shock front and to determine location of the limiting characteristic, the standard scheme is used without setting the back boundary but choosing the last limit on each step to lay within the domain of dependence of the solution already determined. Due to the complexity of two-dimensional interpolation in this scheme, the re-evaluation of the properties on each constant time line is omitted.

As the exact third order solutions diverge very rapidly for weak initiation, attention was first placed on the range of validity of the third order solution as the initial data. It was first believed that the starting distance from the chamber wall would have to be correspondingly small. It was, however, subsequently found that the numerical results quickly converged to the same unique solution even though large starting distances, that is regions where the third order solution is not valid, were employed.

The accuracy of both characteristic methods, i.e. standard and Hartree constant time line, were also investigated with respect to space and time mesh size.

From the numerical solutions, shock trajectory, the limiting characteristic, the limiting similarity line and two kinds of singularity lines were evaluated. Also pressure and density gradient variation on the shock front, local energy distributions and values of θ on each shock radius were determined. Three important mathematical points were

also determined; namely, the point where the limiting characteristic develops, the point on the shock trajectory where the shock acceleration becomes zero, and the point where the limiting characteristic, singularity line and the limiting similarity line join together to initiate a similarity zone. From those and energy considerations, the self-amplifying mechanisms and "forgetfulness" of initial conditions were investigated.

By a "least squares fit" along the trajectory where the similarity solution is supposed to be satisfied, the index of the power law trajectory and the factor A were determined for several different initial conditions.

CHAPTER II

FORMULATION

2.1 Model, Basic Equations and Boundary Conditions

Among three basic shock generating mechanisms: namely, the energy-driven fixed-wall model, the piston-driven shock model and the pressure-driven diaphragm model, the first model of impulsively generated energy-driven shock is considered neglecting the effects of any confining walls as well as effects of viscosity and heat transfer.

Consider a spherical or cylindrical wall of radius $R_{_{\scriptsize O}}$ containing perfect gas with constant specific heat ratio , constant initial pressure $p_{_{\scriptsize O}}$ and density $\rho_{_{\scriptsize O}}$. Releasing energy $E_{_{\scriptsize O}}$ instantaneously at the wall (time t=0, radius $r=R_{_{\scriptsize O}}$), a strong shock is generated which collapses towards the center of symmetry through the gas originally at rest, where $E_{_{\scriptsize O}}$ is the total released energy for the spherical case, per unit length for the cylindrical case.

Since the energy is released instantaneously in a vanishingly thin cylindrical ring or spherical shell, the energy density at the first moment is always infinite so that a strong shock is generated irrespective of $\mathbf{E}_{\mathbf{O}}$. The weaker the initial energy, the faster the shock strength dies out.

The governing conservation equations for the motion of the shocked gas are:

$$\frac{\partial f}{\partial t} + \frac{\partial \rho u}{\partial r} + \frac{j\rho u}{r} = 0 \tag{2.1}$$

$$\frac{\partial u}{\partial t} + u \frac{\partial u}{\partial r} + \frac{1}{\rho} \frac{\partial p}{\partial r} = 0 \tag{2.2}$$

$$\left(\frac{\partial}{\partial t} + u \frac{\partial}{\partial r}\right) \frac{p}{p^r} = 0 \tag{2.3}$$

where j = 1 for cylindrical symmetry,
j = 2 for spherical symmetry.

The boundary conditions at the normal shock front are:

$$\frac{\ell_s}{\ell_o} = \frac{\delta + 1}{\delta - 1 + 2/M_s^2} \tag{2.4}$$

or
$$\frac{C_s}{\dot{R}_s} = \sqrt{(2\chi - (\delta - 1) \cdot \frac{1}{M_s^2})(\chi - 1 + 2/M_s^2)}$$
 (2.5)

$$\frac{u_s}{R_s} = \frac{2}{r+1} \left(1 - 1/M_s^2 \right) \tag{2.6}$$

$$\frac{r_{s}}{r_{s}^{2}} = \frac{2}{r+1} - \frac{r-1}{r(r+1)M_{s}^{2}}$$
 (2.7)

where $R_s = \frac{dR_s}{dt}$ is shock velocity,

 $\boldsymbol{c}_{o},\;\boldsymbol{\rho}_{o},\;\boldsymbol{p}_{o}$ are sound speed, density and pressure of the undisturbed medium,

 $c_{_{\rm S}},~u_{_{\rm S}},~\rho_{_{\rm S}},~p_{_{\rm S}}$ are sound speed, particle velocity, density and pressure immediately behind the shock front, respectively,

and

$$M_s = \frac{\dot{R}_s}{C_o} = \frac{\dot{R}_s}{\sqrt{\sigma P_o/\rho_o}}$$
 (2.8)

is the shock Mach number.

The only boundary condition on the wall is:

$$u(R_0, t) = 0$$
 for all t.

2.2 <u>Initial Starting Data</u>

For the pressure-driven diaphragm model or the piston-driven shock wave model, one may carry out the numerical calculations throughout the collapse from the starting point singularity to the end of collapse without resorting to the use of special starting data. This is due to the existence of the moving physical back boundary, that is, the contact surfaces in the diaphragm model, piston trajectory in the piston-driven model, which assure proper magnitude of density or sound speed to guarantee suitable stability for the early stage before developing the limiting characteristic.

For the energy-driven shock model, however, it is difficult to determine accurate initial starting data by the characteristic method since near the fixed wall the density goes to zero, and thus the sound speed tends to infinity so that the numerical calculations are unstable regardless of time mesh size.

To avoid this difficulty, one may set an arbitrary back boundary neglecting the effect of fluid properties near the wall. This kind of effect may be neglected if calculation starts when the limiting characteristic develops. It is quite clear that one cannot neglect the effect of fluid properties near the wall at the early stage since the magnitude of fluid properties are all very large.

Thus in the present calculation, analytical third order solutions are used to determine initial data.

To achieve analytical third order solutions, the variables are non-dimensionalized following Bach and Lee as:

$$g = (r - R_o) / (R_s - R_o)$$
 (2.9)

$$\chi_{s} = R_{s} - R_{o} \tag{2.10}$$

$$x_s = X_s/R_o = (R_s - R_o)/R_o \qquad (2.11)$$

and the functions are defined as:

$$\Psi(\xi, x_s) = e(r, t)/e_s$$
 (2.12)

$$\phi(\xi, x_s) = u(r, t) / \dot{\chi}_s(t)$$
 (2.13)

$$f(\xi, x_s) = p(r, t)/c \dot{x}_s^2(t)$$
 (2.14)

where
$$\dot{X}_s = \frac{dX_s}{dt} = \dot{R}_s$$
.

Then the basic governing equations (2.1) to (2.3) become:

$$(\phi - \xi) \frac{\partial \psi}{\partial \xi} + \psi \frac{\partial \phi}{\partial \xi} + \frac{j \phi \psi x_s}{1 + x_s \xi} = -x_s \frac{\partial \psi}{\partial x_s}$$
 (2.15)

$$(\phi - \xi) \frac{\partial \phi}{\partial \xi} + \theta \phi + \frac{1}{\psi} \frac{\partial f}{\partial \xi} = -x_s \frac{\partial \phi}{\partial x_s}$$
 (2.16)

$$(\dot{\psi} - \xi) \frac{\partial f}{\partial \xi} + \sigma f \frac{\partial \phi}{\partial \xi} + 2\theta f + \frac{j r \phi f x_s}{1 + x_s \xi} = -x_s \frac{\partial f}{\partial x_s}$$
 (2.17)

where

$$\theta = x_s \dot{x}_s / \dot{x}_s^2 \qquad (2.18)$$

and \dot{x}_s , \ddot{x}_s denote first and second derivatives of x_s with respect to time t.

Non-dimensionalizing time t as:

where energy-reduced characteristic time t_j^* which can be interpreted as an order of magnitude of the total collapsing time, defined as:

$$t_{j}^{+} = \left(\frac{P_{o} K_{j} R_{o}^{j+3}}{(j+1) E_{o}}\right)^{1/2}$$
 (2.20)

where
$$k_j = 2\pi$$
 for $j = 1$
 $k_j = 4\pi$ for $j = 2$.

Then the shock wave velocity and sound speed can be written, respectively, as:

$$\dot{R}_{s} = \frac{dR_{s}}{dt} = \dot{X}_{s} = R_{o}\dot{x}_{s} = \frac{R_{o}}{t_{s}^{*}}\frac{dx_{s}}{d?} = \frac{R_{o}}{t_{s}^{*}}\dot{x}_{s}(?) \qquad (2.21)$$

$$C_{j}^{*2} = C_{0}^{2} t_{j}^{*2} / R_{0}$$
 (2.22)

and the energy integral can be written as:

$$1 = x_s \cdot \dot{x}_s^2(\gamma) \cdot (j+1) \cdot I(x_s) - C_j^{*2} \frac{(1-(1+x_s)^{j+1})}{\gamma(\gamma-1)}$$
 (2.23)

where

$$I(x_s) = \int_{1}^{0} \left(\frac{f}{\sigma - 1} - \frac{\psi \phi^2}{2}\right) \left(1 + x_s \xi\right) d\xi$$
 (2.24)

The value of c_j^{*2} represents the inverse of the intensity of initial energy release. The larger the initiation energy, the smaller c_j^{*2} becomes. If $E_o \rightarrow \infty$, then $t_j^* \rightarrow 0$, thus $c_j^{*2} \rightarrow 0$, the strong shock is maintained throughout the collapse. For example, an initiation of 10 joules energy gives a value of $t_2^* = 12.5 \times 10^{-6}$ sec and $c_2^{*2} = 0.0196$ in a spherical chamber of radius 3 cm. containing air at 10 mm Hg of initial pressure.

As the early phases of collapse $|x_s| \ll 1$, one may seek the solution in the following power series:

$$\psi(\xi, \chi_s) = \sum_{n=0}^{\infty} \psi^{(n)}(\xi) \cdot \chi_s^n$$

$$\phi(\xi, \chi_s) = \sum_{n=0}^{\infty} \phi^{(n)}(\xi) \cdot \chi_s^n$$
(2.25)

$$f(\xi,\chi_s) = \sum_{n=0}^{\infty} f^{(n)}(\xi) \cdot \chi_s^n \qquad (2.25)$$

From the energy integral (2.23), one can see that $\dot{x}_{_{\rm S}}(?)$ should satisfy:

$$\dot{x}_s(7) = \frac{1}{x_s} \sum_{n=0}^{\infty} F_n x_s^n \qquad (2.26)$$

and so can readily determine θ as:

$$\Theta(x_s) = \sum_{n=0}^{\infty} \Theta^{(n)} x_s^n$$
 (2.27)

where the coefficients $\theta^{(n)}$ are given as:

$$\Theta^{(0)} = -1/2$$

$$\theta^{(1)} = F_1 / 2F_0,$$

$$\theta^{(2)} = F_3/F_0 - F_1^2/2F_0^2$$

$$\theta^{(3)} = \frac{1}{2} \left((F_1/F_0)^3 - 3F_1F_2/F_0^2 + 3F_3/F_0 \right)$$

Substituting the perturbation expressions obtained from Equations (2.25) to (2.27) into the conservation equations (2.15) to (2.17), one can obtain nth order solution with boundary conditions at the shock $\xi = 1$. (For the detailed derivation see Bach and Lee, 1967.)

2.3 Characteristic Equations

For the convenience of the numerical calculation and to drop out the parameter θ from the governing equations, space variable and functions are redefined as:

$$r' = r / R_0 \tag{2.28}$$

$$R_s' = R_s / R_o \tag{2.29}$$

$$\dot{R}'_s(7) = \frac{d}{d7}(R_s/R_o) = \dot{x}_s(7) \tag{2.30}$$

$$e'(r',7) = e(r,t)/e_o = \psi(\xi,x_s)$$
 (2.31)

$$u'(r',7) = u(r,t) \left\langle \frac{R_0}{t_j^*} \right\rangle = \dot{x}_s(7) \cdot \phi(\xi, x_s) \quad (2.32)$$

$$p'(r',7) = p(r,t)/e_0 \left(\frac{R_0}{t_j^2}\right)^2 = \dot{x}_s^2(7) f(\xi,x_s) \qquad (2.33)$$

$$C'(r',7) = \sqrt{rp'/e'}$$
 (2.34)

Then the basic conservation equations can be written as:

$$\frac{\partial \ell'}{\partial 7} + \frac{\partial \ell' u'}{\partial r'} + \frac{j \ell' u'}{r'} = 0 \qquad (2.35)$$

$$\frac{\partial u'}{\partial 7} + u' \frac{\partial u'}{\partial r'} + \frac{1}{\ell'} \frac{\partial p'}{\partial r'} = 0 \qquad (2.36)$$

$$\left(\frac{\partial}{\partial 7} + u'\frac{\partial}{\partial \Gamma'}\right)\frac{p'}{e^{r}} = 0 \tag{2.37}$$

and normal shock relations become:

$$e_s' = \frac{r+1}{r-1+2/M_s^2}$$
 (2.38)

or
$$C_s' = \frac{\sqrt{(2\sigma - (\nabla - 1) \cdot 1/M_s^2)(\nabla - 1 + 2/M_s^2)}}{\nabla + 1} \dot{x}_s(7)$$
 (2.39)

$$u'_{s} = \frac{2}{s+1} (1 - 1/M_{s}^{2}) \dot{x}_{s}(7)$$
 (2.40)

$$\phi'_{s} = \left(\frac{2}{r+1} - \frac{r-1}{\gamma(r+1)M_{s}^{2}}\right) \dot{z}_{s}^{2}(7)$$
 (2.41)

where

$$M_s^2 = \dot{R}_s^2/c_o^2 = \dot{x}_s^2(7)/c_j^{*2}$$
 (2.42)

From the hyperbolic conservation equations we can obtain the following characteristic equations:

Physical Characteristic Equations

$$\frac{dr'}{dr} = u' + C'$$

$$\frac{dr'}{d?} = u' - c'$$

$$\frac{dr'}{dr} = u'$$

State Characteristic Equations

$$du' = -\frac{c'}{\tau p'} dp' - \frac{j u'c'}{r'} dr$$

$$du' = \frac{c'}{rp'}dp' + \frac{ju'c'}{r'}dr$$

$$\frac{C'}{C'_o} = \left(\frac{p'}{p'_o}\right)^{\frac{p-1}{2q}}$$

Equations (2.43) to (2.48) consist of the basic equations for the

further numerical calculations in the method of characteristics.

CHAPTER III

NUMERICAL ANALYSIS

In the method of characteristics the six basic characteristic equations are put into finite difference forms, such as: along positive characteristics C^{\dagger} ,

$$\Delta r' = (\bar{u}' + \bar{c}') \Delta \gamma \tag{3.1}$$

$$\Delta u' = -\frac{1}{\delta} \left(\frac{\bar{c}'}{\bar{p}'} \right) \Delta p' - j \left(\frac{\bar{u}' \bar{c}'}{\bar{r}'} \right) \Delta 7 \tag{3.2}$$

along negative characteristics C,

$$\Delta \Gamma' = (\bar{u}' - \bar{C}') \Delta 7$$
 (3.3)

$$\Delta u' = \frac{1}{r} \left(\frac{\overline{c'}}{\overline{p'}} \right) \Delta p' + j \left(\frac{\overline{u'} \, \overline{c'}}{\overline{r'}} \right) \Delta 7 \tag{3.4}$$

along particle paths Co,

$$\Delta r' = \overline{u'} \Delta 7$$
 (3.5)

$$\frac{C'}{C'_o} = \left(\frac{p'}{p'_o}\right)^{\frac{\chi-1}{2\delta}} \tag{3.6}$$

where \bar{r}' , \bar{u}' , \bar{p}' and \bar{c}' represent arithmetic means between two points along the particular characteristic line.

For the energy-driven shock model the starting data on the first constant time line were calculated from the analytical third order solutions. It was found, using various starting points, that $R_{\rm s}/R_{\rm o}=$.90 yielded satisfactory results for a great variety of energy release and was therefore used in all of the numerical calculations.

The starting condition taken at $R_s/R_o=0.8$ was applied for strong initiation ($c_j^{*2}=0$) in the standard scheme, and the results are compared with that of the main starting condition ($R_s/R_o=0.9$) in Fig. 15. Considering the close agreement between them, one can assume that the starting data taken at $R_s/R_o=0.9$ will give agreeable results for strong initiation. For the weak initiation, the perturbation solution is an asymptotic series on x_s and diverges rapidly. Hence two numerical calculations were first carried out for $c_j^{*2}=1$ with the starting point at $R_s/R_o=0.9$ and $R_s/R_o=0.97$. Both results, as we see from Figs. 13 and 14, coincide surprisingly well in several time steps of numerical calculation in spite of such big errors which were initially imposed on the shock front by the third order solution taken at $R_s/R_o=0.9$. The foregoing converging process may be one of the surprising properties of imploding shock problems. Through the analysis one can

therefore expect fairly good results taking initial starting data at $R_s/R_o = 0.9$, even for the weak initiation of $c_j^{*2} = 1$.

In Hartree's scheme, one of the merits is comparatively accurate and easy interpolation. The stability criterion of the method can be assured by the Courant condition (Courant and Friedrichs, 1948).

$$\Delta 7 \langle \Delta r'/c' \rangle$$
 (3.7)

This criterion gives maximum time mesh size which guarantees both feet of the characteristics drop in a zone of neighbouring mesh points (between points 1 and 2 in Fig. 3.1). The time mesh size \triangle ? is evaluated for each new time line at the back boundary of the old time line. Near the wall, due to the large values of sound speed, it is difficult to evaluate the fluid properties under the above stability criterion. However, the particle velocity is zero at the wall; the pressure has zero gradient there; the evaluation of the variables near the wall is not too important.

In addition, in the implosion problem, the limiting characteristic has already developed and is present in the initial data at $R_{\rm s}/R_{\rm o}=0.9$. This limiting characteristic rapidly approaches the shock front after several time steps of calculation and so the evaluation of the region close to the wall has no effect at all on the subsequent shock motion although it has a small effect in the region behind this characteristic line. Therefore, we can set arbitrary back boundary without losing any accuracy to carry on the whole calculation so long as the back boundary

is set outside the limiting characteristic.

Thus the back boundary is introduced near the wall by the relations:

$$r_b' = 0.72 (1 - R_s')$$
 (3.8)

It covers three-quarters of the whole range of shocked gas on each time line. It also gives fairly good distance which closes enough to keep the advantage of using the boundary condition $\mathbf{u'}=0$ at the wall for later interpolation, since the correct boundary condition requires one of the three dependent variables be specified on the back boundary. The back boundary is located outside the limiting characteristic which assures the accuracy of numerical results for the dependent domain. Thus the main calculations are carried on from the shock front to the back boundary on each successive time line starting from $R_{\rm g}/R_{\rm o}=0.9$ (Fig. 16).

3.1 Hartree's Constant Time Line Scheme

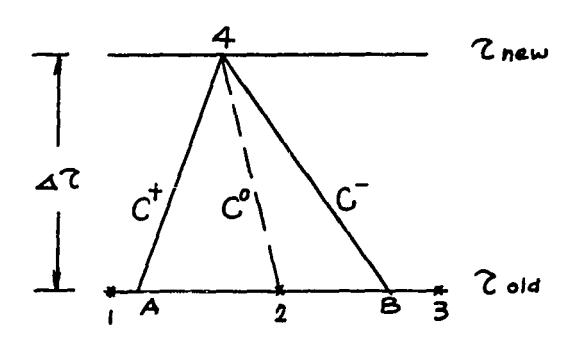


Fig. 3.1

In Hartree's scheme numerical calculations are carried on along each particle path \boldsymbol{C}^{0} on the successive constant time line. Therefore, all the variables can be determined through one-dimensional interpolation.

The numerical calculation is carried out in such a way that; first, from each mesh point (say pt. 2 in Fig. 3.1) on the known old time line build a particle path and determine pt. 4 on the new time line; second, from pt. 4 build both C⁺ and C⁻ characteristics back to the old time line and find points A and B on the old time line; third, iterate till all the variables and functions on the pts. 4, A and B satisfy the six basic characteristic equations and interpolation relationships. One always has to establish the same number of independent equations as the number of unknowns on those points. Thus the problem is analogous to solve n simultaneous algebraic equations with n unknowns.

In general, there are five different cases to carry on the calcu-

lations for:

- i) the interior flow mesh points,
- ii) the points on the shock front,
- iii) the mesh points built immediately behind the shock by the new particle path which originated newly from the shock front on the old time line,
- iv) the points on the back boundary, and
- v) the mesh points just in front of the back boundary.

For the interior flow mesh points (Fig. 3.1), one has to determine r_4' , u_4' , p_4' and c_4' which should satisfy the six basic characteristic equations (3.1) to (3.6). To solve the basic equations, we have to evaluate \bar{r}' , \bar{u}' , \bar{p}' and \bar{c}' , i.e. r_A' , u_A' , p_A' , c_A' and r_B' , u_B' , p_B' and c_B' . Since we are given all the variables on the mesh pts. 1, 2 and 3, we can interpolate those variables from pts. 1, 2 and 3.

Particle velocities \mathbf{u}_{A}^{\prime} and \mathbf{u}_{B}^{\prime} are interpolated linearly, but pressures and sound speeds are interpolated quadratically in such a way that:

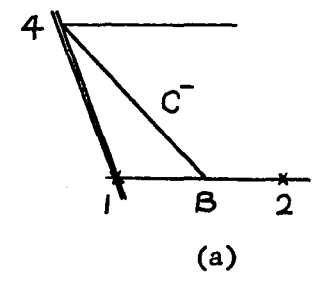
$$G - G_2 = a(r'-r'_2)^2 + b(r'-r'_2)$$
 (3.9)

where G represents u', p' and c' to be interpolated,

- G_2 represents u_2' , p_2' and c_2' which are known,
- a, b are constants which must be determined on each mesh point from the variables of the pts. 1, 2 and 3.

Thus we have twelve independent equations, i.e. six basic characteristic equations and six interpolation formulae to solve twelve unknowns.

Assuming trial values of the unknowns, first approximation can be carried out, and with repeated iterations we may find exact solutions. Iterations are repeated until the differences of u_4' , p_4' and c_4' from two successive values are below a desired limit. Throughout the calculation it was found that three iterations were sufficient to keep this difference less than .00005.



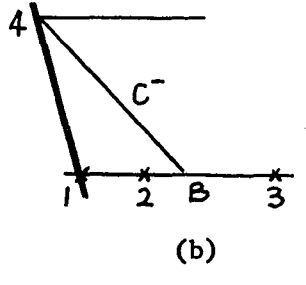


Fig. 3.2

For the points on a shock front, one has to determine R_s' , $\dot{x}_s(?)$, u_4' , p_4' and c_4' . Two characteristic equations along C characteristic and four normal shock relations, i.e. (2.39), (2.40), (2.41) and

$$\Delta R_{s}' = \dot{x}_{s}(?) \Delta ? \qquad (3.9')$$

can be used to solve the problem.

To evaluate mean value terms, we have to know four additional unknowns r_B' , u_B' , p_B' and c_B' of pt. B (Fig. 3.2). Now we have nine unknowns with nine equations including three more interpolation formulae.

There are two possible cases (a) and (b) in Fig. 3.2. For the case (a) linear interpolations are adopted and for the case (b) quadratic interpolations are used for all three functions u_R' , p_R' and c_R' .

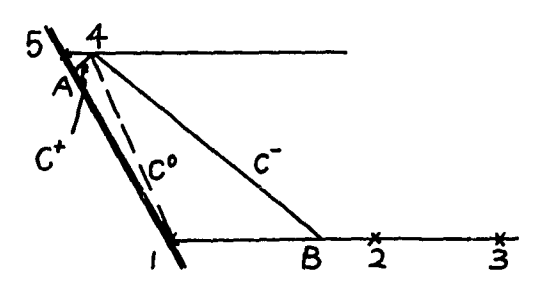


Fig. 3.3

To keep approximately the same number of mesh points on each successive time line, new particle paths are set from the shock front on the old time line whenever the condition $|\mathbf{r}'_2 - \mathbf{r}'_1| \geqslant |\mathbf{r}'_3 - \mathbf{r}'_2|$ is observed. As will be seen in Chapter IV, this procedure gives the most important merit for Hartree's scheme in the implosion problem. As the new particle path set a mesh point so close to the shock front on the new time line, this new mesh point may never fail to detect positive pressure gradients behind the shock, however narrow it is, without paying any additional machine time. For this new pt. 4, the calculations are the same as the one for the interior points except to

interpolate r_A' , u_A' , p_A' and c_A' from two shock front points 5 and 1 on the new and old time lines. Therefore, the calculation of this point must be carried on after the variables on pt. 5 are evaluated. In this case, we have additional unknown 7_A .

To solve the problem for the points on the back boundary, one of the dependent variables, in addition to the locus of the boundary, must be defined beforehand.

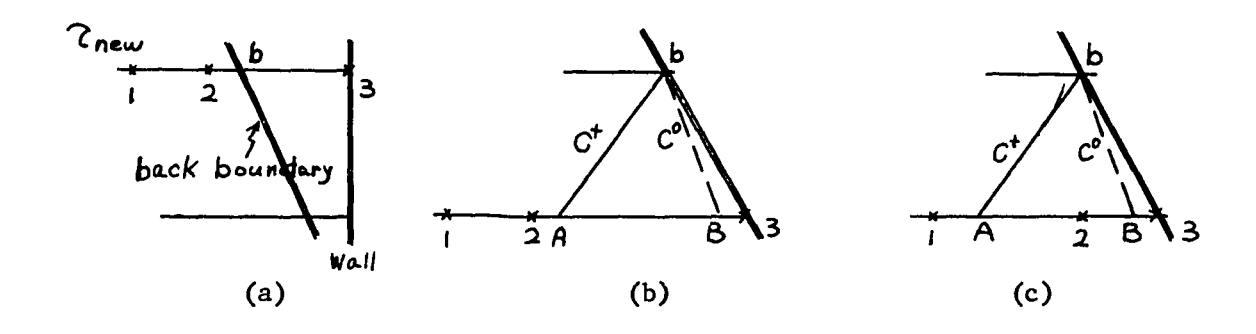


Fig. 3.4

 r_b' can be evaluated exactly from Equation (3.8). u_b' can be determined interpolating quadratically from pts. 1, 2 for which variables are already evaluated and pt. 3 (Fig. 3.4, a) where $u_3' = 0$ from boundary conditions.

Therefore, for the mesh points on the back boundary, we have only two main unknowns p_b^i and c_b^i in addition to eight temporary unknowns r_A^i , u_A^i , p_A^i , c_A^i , r_B^i , u_B^i , p_B^i and c_B^i (Fig. 3.4a, b). On the other hand, as we have four basic characteristic equations along C^+ and C^0 , and six interpolation formulae from the points 1, 2 and 3, the problem can be

solved.

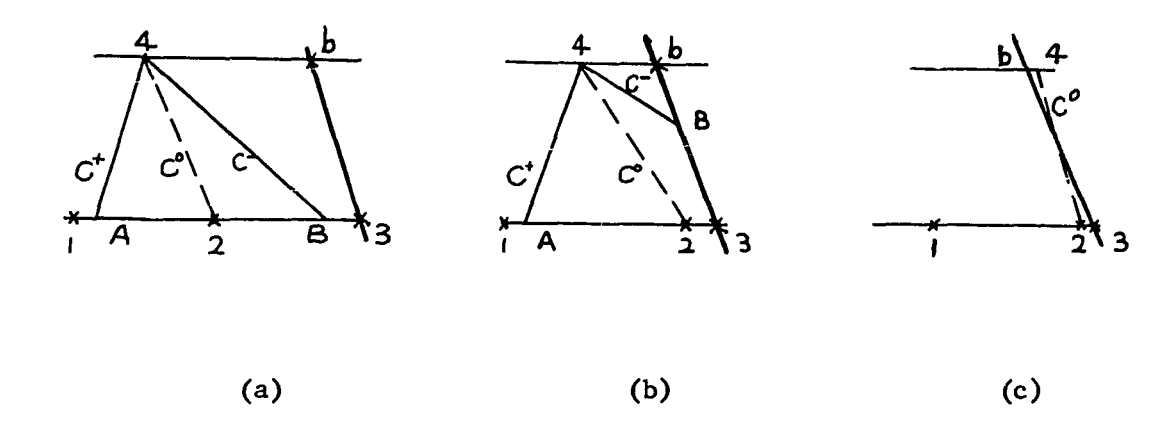


Fig. 3.5

When we evaluate variables for the mesh points just in front of the back boundary, we have three different cases. Case (a) corresponds to the usual interior flow mesh point and can be evaluated in the usual way. Case (c), where pt. 4 appears behind the back boundary, we just cancel the calculations. The canceled mesh point at this back boundary may be compensated at the shock front so that the scheme can keep approximately the same number of mesh points on successive time lines. Case (b), we have to interpolate r_B^i , r_B^i , r_B^i , r_B^i and r_B^i from the variables of pts. b and 3 on the back boundary. Therefore, the calculation for this case should be proceeded after the variables of pt. b are evaluated.

3.2 Standard Characteristic Method

Applying the standard scheme mainly to check the accuracy of Hartree's results especially on the shock front and to determine the limiting characteristic line, the numerical calculations are carried on from the shock front to the last characteristic, which was initiated on the wall at the initial starting time line. The total number of mesh points, therefore, decreases one in every other time step (Fig. 16). This saves considerable machine time without losing any accuracy of the shock wave properties, since the last characteristic is located behind the limiting characteristic.

There are two different cases for the numerical calculation: for the interior flow mesh points and for the points on the shock front.

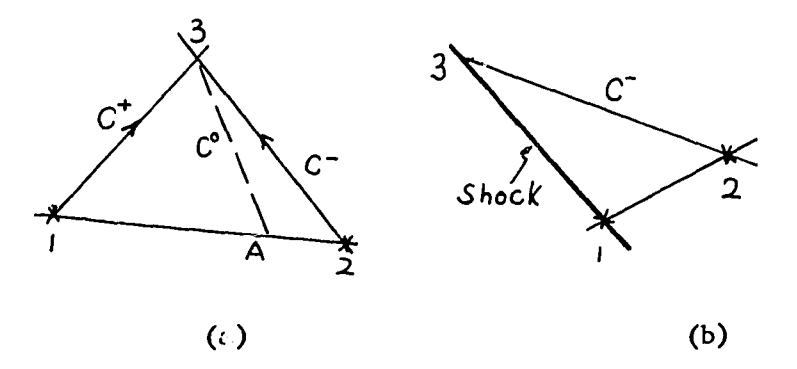


Fig. 3.6

In the standard scheme, we issue both C⁺ and C⁻ characteristics from pt. 1 and pt. 2 to determine pt. 3 (Fig. 3.6a) and then draw backwards a particle path from pt. 3 to determine pt. A. Therefore,

we have ten unknowns, t_3' , r_3' , u_3' , p_3' , c_3' , t_A' , r_A' , u_A' , p_A' and c_A' to be determined. On the other hand, we have ten equations, i.e. six basic characteristic equations, (3.1) to (3.6), and four linear interpolation formulae.

For the points on the shock front, the evaluation is carried on in every other time step. We have six quantities t_3' , r_3' , u_3' , p_3' , c_3' and $\dot{x}_{s(?)}$ to be determined, and exactly six equations can be used, namely, two characteristic equations (3.3) and (3.4), three normal shock relationships (2.39) to (2.41), and the definition of shock wave velocity (3.9).

In the standard scheme, all the new points are evaluated from the known points within the exact domain of dependence. In this sense, one may expect more accurate results in this scheme than Hartree's. However, due to the complexity of two-dimensional interpolation, only linear interpolation can be applicable, consuming much more time than that of Hartree's quadratic interpolations. Considering these merits and shortages in both schemes, one may expect the same order of accuracy, and Chou (1966, 1967) has shown the fact from his numerical calculation in explosion problems.

3.3 Similarity Conditions

For similarity solutions to exist, in general, the following conditions should be satisfied for the basic governing equations, boundary conditions, initial conditions and thermodynamic conditions.

i) The basic partial differential equations can be reduced to

a set of ordinary differential equations with respect to a similarity variable:

$$\xi_{s} = r/R_{s} = r'/R'_{s}$$
 (3.10)

It leads us to have the first condition, the so-called power law trajectory.

$$R_{s} = A(t_{c} - t)^{N}$$
or
$$R'_{s} = A'(t'_{c} - t')^{N}$$
or
$$R'_{s} = A''(7_{c} - 7)^{N}$$
where
$$t' = tC_{o}/R_{o}.$$
(3.11)

From this we have the second condition.

$$\Theta_{R_s} = \frac{R_s \dot{R}_s}{\dot{R}_s^2} = \frac{N-1}{N} = \text{constant}$$
 (3.12)

or

$$\Theta_{R_s} = \frac{1 + x_s}{x_s} \frac{x_s \ddot{x}_s}{\dot{x}_s^2} = \frac{1 + x_s}{x_s} \Theta_{x_s} = \text{constant}$$
(3.13)

where A, A', A" and N are constants and t_c , t_c' or c are the total collapsing time.

Guderley and Butler evaluated this value, for $\gamma = 1.4$, j = 2, as:

$$N = 0.717173 \tag{3.14}$$

$$\theta = -0.394 \tag{3.15}$$

Since $x_s = -1$ at the center, for θ_{x_s} we have:

$$\theta_{x_s} \rightarrow \infty$$
 , if $x_s \rightarrow -1$ (3.16)

ii) The boundary conditions on the shock front give us the third condition:

$$M_s \longrightarrow \infty$$
 (3.17)

- iii) For the initial condition, the counterpressure effect should be negligible and it leads to the condition (3.17) in implosion problems.
- iv) From the thermodynamic similarity condition, the equation of state should have the form:

$$e = pF(p) \tag{3.18}$$

If we can assume the similarity variable as:

$$\xi_s = \Gamma'/R'_s = constant$$

then Equation (3.18) is satisfied as:

$$e = \frac{1}{\gamma - 1} \frac{\gamma}{\ell} \tag{3.19}$$

For $\gamma = 1.4$, j = 2, the limiting similarity variable was calculated as:

$$\xi_{s}^{*} = 1.12$$
 (3.20)

It leads to the fourth condition to have the similarity solution.

3.4 Singularity Analysis

With all the requirements for the similarity solution satisfied, the basic conservation equations can be written in ordinary differential equations as:

$$\frac{d\Psi}{d\xi_{s}} = \frac{(\phi - \xi_{s}) \theta_{RS} \Psi \phi - 2\theta_{Rs} f - j(\phi - \xi_{s})^{2} \phi \Psi/\xi_{s}}{(\phi - \xi_{s}) \left[(\phi - \xi_{s})^{2} - \partial f/\Psi\right]}$$
(3.21)

$$\frac{d\Phi}{d\xi_s} = \frac{-(\phi - \xi_s)\Theta_{Rs} + 2\Theta_{Rs}f/\psi + j s f \Phi/\xi_s \psi}{(\phi - \xi_s)^2 - s f/\psi}$$
(3.22)

$$\frac{df}{d\xi_s} = \frac{f\left[-(\phi - \xi_s)(2\Theta_{Rs} + j\gamma\phi/\xi_s) + \gamma\Theta_{Rs}\phi\right]}{(\phi - \xi_s)^2 - \gamma f/\psi}$$
(3.23)

By now, there is no difference between implosion and explosion.

The above equations satisfy for both cases. Singularity occurs usually at singular points of the governing differential equations. From the above equations we have three kinds of singular points:

$$\xi_s = \Phi \tag{3.24}$$

$$\xi_s = \phi \pm \sqrt{vf/\psi}$$

However, in implosion problems, we have:

$$| \xi \xi_s | \leq \infty$$
 (3.25)

and
$$\xi_s \neq \Phi$$

Therefore, the only singularity in this case is:

$$\xi_s = \phi - \sqrt{\sigma f/\psi} = (u'-C')/\dot{x}_s(7) \tag{3.26}$$

On the other hand, from the similarity condition, we have:

$$r' = g_s R_s' = constant \cdot R_s'$$
 (3.27)

Differentiating Equation (3.27) with respect to ? and substituting singularity condition (3.26), we get:

$$\frac{dr'}{d\hat{c}} = \xi_s \, \dot{R}'_s(7) = \xi_s \, \dot{x}_s(7) = u' - c'$$

i.e.
$$\frac{dr'}{d?} = u' - C' \qquad (3.28)$$

This simply means that for the similarity solution to exist, the limiting similarity line $\S_S^* = 1.12$ should coincide with a singularity line, and the line should be a characteristic. We call this particular characteristic the limiting characteristic line.

Therefore, we have four conditions to determine the similarity zone.

- i) A similarity solution starts at time 7₅ (Fig. 7) where the singularity line, the similarity line and the limiting characteristic line join together and merge into the center of collapse as a line hereafter.
- ii) From 7_5 to 7_c , $\theta_{RS} = -0.394$ (Eq. 3.15) should be satisfied.
- iii) Strong shock condition should be held, i.e. $M_s \longrightarrow \infty$.
- iv) The shock trajectory should follow the power law (Eq. 3.11).

To determine the similarity parameters N, A' or A" and t_c or c_c , steepest descent method is applied on the points along the shock trajectory where the similarity solution is valid.

To investigate the property of forgetfulness and the selfamplifying mechanism, other singular points:

$$\phi - \sqrt{rf/\psi} = \xi_s = 1$$

or

$$u'-c'=\dot{x}_{s}(?) \tag{3.29}$$

are considered. As the energy consideration may give physical interpretation on the mechanism, the pressure and density gradients and kinetic thermal-pressure energy density distributions are evaluated on each time step. The energy distributions on each particular line and energy peak are plotted and compared (Figs. 8 and 9). Local energy density may be written by:

$$\mathcal{E} = \mathcal{E}_{\tau} + \mathcal{E}_{\kappa} = \frac{f}{r-1} - \frac{\psi \phi^2}{2} \qquad (3.30)$$

where

 ξ_{τ} : thermal-pressure energy

 $\mathcal{E}_{\mathbf{K}}$: kinetic energy.

CHAPTER IV

RESULTS AND DISCUSSION

4.1 On the Numerical Schemes

i) Starting Data

For strong initiation (0 \leq $c_j^{*2} \leq$ 0.1), the analytical third order solution provides sufficiently accurate initial data at R_s/R_o = 0.9 in magnitude and profile. Two sets of numerical results using initial data at R_s/R_o = 0.8 and R_s/R_o = 0.9 were plotted in Fig. 15. The figure shows almost perfect coincidence between them.

The third order solution itself can explain the motion fairly well in the early stage for about one third of the total range. The shock trajectory until $R_s/R_o=0.4$, the shock velocity until $R_s/R_o=0.5$ (Fig. 1), and the various profiles until $R_s/R_o=0.7$ (Figs. 3, 4 and 5) agree very closely with numerical solutions.

For weak initiation (1 \leq c $_{j}^{*2}$), however, the perturbation solutions diverge very rapidly, and the range of validity seems to be highly limited. The third order solution gives excessive values as a whole at $R_{s}/R_{o}=0.9$, the particle velocity and the density are negative ($\Phi=-5.49$, $\Psi=-0.198\times10^4$) on the shock front. Even at $R_{s}/R_{o}=0.97$, density at the shock front has a large error (Fig. 14). High pressure and density peaks behind the shock were observed at a very early stage. Profiles look like usual profiles in the shrunk

space coordinate.

Two sets of numerical results using initial data at $R_s/R_o=0.9$ and 0.97 are plotted in Figs. 13 and 14. In spite of such a large difference in initial data, both results match surprisingly well only after several runs of numerical calculation.

This rapid correction of the error of the initial data seems to be due to the rapid re-distribution of the local energy through proper treatment of the motion, which is characterized by the self-amplification and forgetfulness of the initial condition by the numerical procedure. Between $R_0^* \sim R_1^*$ (Fig. 14), the motion temporarily becomes a highly self-propagating due to the poorly evaluated local energy peak behind the shock front which is initially imposed by the perturbation solution (at R_1^* the energy gradient of the shock becomes zero). At this moment, as the area effect (at the shock surface) is still small comparing to the volume (between shock and the wall) effect in the real motion (Fig. 17), the corrected motion becomes again decelerative, and the local energy distribution becomes close to the proper one.

Therefore, in spite of the fact that the third order solution itself cannot treat the motion properly at the very early stage for weak initiation, so long as the total energy is conserved, it may provide fairly good initial data at $R_{\rm g}/R_{\rm g}=0.9$ for further numerical calculations. Thus one may note this fact as a peculiar but convenient nature of the implosion problem in numerical calculations.

ii) Mesh Size

To check the mesh size effect, three different mesh sizes were used on the first time line, \triangle $(r/R_0) = 0.001$ and 0.0002 for the standard scheme, \triangle $(r/R_0) = 0.001$ and 0.0016 for Hartree's scheme, and the results were plotted for $c_j^{*2} = 0$ in Fig. 1. It took 90 minutes for a calculation when mesh size \triangle $(r/R_0) = 0.0002$ was used and 10 minutes for the other cases.

The figure indicates, however, that each result within the same scheme coincides perfectly. Therefore, one may assure the accuracy by taking the mesh size Δ (r/R_o) = 0.001.

iii) Comparison of Numerical Schemes

Quite contrary to the coincidence of the results between different mesh sizes in the same scheme, there are rather large discrepancies observed between the results of Hartree and standard schemes (Figs. 1 and 2).

Though both results agree qualitatively, such as the infinite trajectory slope at the center, the asymptotic nature of the profiles near the center, the shapes of the curves and complete coincidence at the early stage, quantitative discrepancy beginsto appear at $R_{\rm s}/R_{\rm o}=0.55$ in shock property profiles (Fig. 2), at $R_{\rm s}/R_{\rm o}=0.65$ in the shock velocity and at $R_{\rm s}/R_{\rm o}=0.25$ in the shock trajectory (Fig. 1). As the waves converge to the center, the differences increase except near the center.

Throughout the cases, the standard scheme gives small magnitudes

of shock properties as compared with Hartree's predictions. All these underestimations in the standard scheme are directly connected with the self-amplifying mechanism of the implosion motion which may be explained by the early development of positive pressure and density gradients at the shock (Figs. 8 and 9). That is, the standard scheme has no way of detecting these positive gradients even with a finer mesh size of 0.0002 when they are in a narrow zone ($R_{\rm S}/R_{\rm O}=0.25$ - 0.05), and this leads to underestimation. Near the center, however, the positive gradient zone becomes wider, and so the standard scheme can also account for this effect, so the discrepancy decreases again.

While Hartree's scheme issues new particle paths at the shock front, it is usually close enough to the shock front on the next time line to detect the pressure gradients at the shock front however narrow.

Then how can it be explained the fact that in spite of the early development of the positive pressure gradient ($R_s/R_o=0.65$, Fig. 9), the shock trajectories agree well up to $R_s/R_o=0.3$? It is simply due to the fact that the pressure variable f does not change much at the shock front irrespective of the pressure gradient (Figs. 9 and 2).

Therefore, it seems that Hartree's scheme is absolutely recommendable and accurate for the numerical calculation in the implosion problem, apart from one-dimensionality, satisfactory treatment of a contact surface and rarefaction fan in other means of shock-generating models.

Thus it may be noted as a further important point in the implosion problem that one should pay particular attention so as to detect the

narrow positive pressure and density gradients at the shock in the numerical calculation, whatever method is used.

4.2 <u>Numerical Solutions</u>

All the results presented here are based on calculations using Hartree's scheme, taking initial starting data at $R_s/R_o=0.9$ and first mesh size with $\Delta (r/R_o)=.001$.

i) Shock Properties

The early stage trajectories are quite analogous to the planar blast wave. The weaker the initial energy release, the sooner the shock strength decrease. Approximately half the region with $\theta=0$ at its center the shock trajectories are linear, and $\theta=0$ occurs approximately at $R_{\rm S}/R_{\rm O}=.53$ irrespective of the initiation condition (Table 1). At the center of convergence the infinite slope can be observed.

The weaker the initial energy, the larger the rate of changing shock velocity (Figs. 11 and 12). Curvatures of all the shock property curves are larger if the initiation energy is small (Figs. 2, 10 and 12). It seems that magnitudes are small, but rates of changing are always larger if initiation energy is small so that they assure the asymptotic nature for the similarity solution sooner or later.

ii) Profiles at Different Shock Radii

The positive pressure gradient at the shock appears at $R_s/R_o = 0.66$ irrespective of initiation conditions and keeps it within a very narrow

zone. It increases very slowly until $R_s/R_o = 0.25$ and after that very rapidly up to infinity in the similarity zone (Figs. 3, 8 and 9).

On the singularity line, however, the magnitude of pressure steadily increases to the shock front value at $R_{\rm s}/R_{\rm o}=0.165$ and then follows the similarity law (Fig. 8). One may see that, in this period, the area convergence smoothes the pressure profile especially in the zone enclosed by the shock front and singularity line while keeping the positive pressure gradient zone immediately behind the shock almost constant and narrow so that the curvature of the shock trajectory remains nearly zero.

The density peak appears rather late at $R_s/R_o=0.45$ but steadily increases from the beginning to the limiting value of 21.6 at the center of convergence irrespective of the initiation condition (Fig. 9).

Contrary to the pressure peak, the density peak spreads into a wide zone from the beginning. It leads to rapid increase of the local kinetic energy in the zone enclosed by the shock front and the singularity line (Figs. 5 and 8). This is the reason that even the third order solution can predict the density peak but not the pressure peak greater than that of the shock front comparatively early at $R_{\rm s}/R_{\rm o}=0.6$.

There are no positive particle velocity gradients. There is, however, a distinction between the two zones where θ is positive and negative. In the zone where $\theta < 0$ (i.e. decelerating shock regime, expanding nature of the initial motion dominates), the peak profile becomes gradually less steep and reaches a maximum at $\theta = 0$. In the

zone where $\theta \ge 0$ (i.e. accelerating shock regime, where the self-amplifying effect is dominant), the profile becomes steeper again.

4.3 <u>Self-Amplifying Mechanism</u>, <u>Initial Condition Forgetfulness</u> and Self-Similarity

The essential difference between imploding and exploding shock waves may be represented by the early development of the limiting characteristic. The self-amplifying mechanism, forgetfulness and self-similarity may be partially explained through energy considerations.

The limiting characteristic develops very early between $R_{\rm S}/R_{\rm O}=0.9$ - 0.92 in most cases; the weaker the initiation energy, the earlier in radius, the later in physical time. Once it has developed, it approaches the singularity line very rapidly and finally coincides with the limiting similarity line at the point where similarity is attained.

There are three main factors to be considered in forgetfulness, namely, the form of the initiation motion, the intensity of the initiation energy and the gas substance which bears the initial condition.

At 7_1 , the limiting characteristic develops and forms with the shock front the self-governing domain. Between $7_0 \sim 7_1$, the expanding motion dominates and the area convergence effect is so small that the motion can be approximated by planar strong blast waves (Fig. 7). At the very moment when the shock wave is generated, the shock strength is infinite irrespective of the initiation energy, but the power source is limited by the initial condition and instantaneously loses most of the energy as the initiation energy is being distributed over an

increasing mass of gas. It leads to forget the majority part of the intensity of the initial condition. At the same time, a fixed percentage of the initiation energy is retained in a small region near the shock whose surface area is shrinking with time. This results in the shock separating itself in a way from the main flow and forgetting as it were the actual details of initiation but only retaining memory as to its original magnitude.

The time 7₁, where limiting characteristic starts, may be characterized as the line where the area effect starts to play an important role. At this time a region is formed which I shall call the self-governing domain, and from here on the details of the initial conditions are becoming somewhat forgotten. The decreasing area effect now causes increasing energy density near the shock which restrains the deceleration of the shock wave, which would otherwise decay as a planar blast wave.

At the time 7_2 , the first singular point is observed. Between $7_1 \sim 7_2$ one can note three distinct behaviours. First, the limiting characteristic rapidly approaches the shock front and to a definite distance near $7 = 7_2$ and thereafter approaches the shock more slowly. This has the effect of producing a similarity nature to the flow behind the shock quite quickly. Second, the distance between the limiting characteristic and the limiting similarity line ($\frac{1}{5_3} = \frac{1}{2} - \frac{1}{2$

and thus analytical approximation for the similarity solution (of Guderley) would be expected to break down at this point. Third, the local energy distribution near the limiting characteristic has a minimum (Fig. 8).

At the time $?_3$ the second kind of singularity first appears. At this point there develops the first physical characteristic which has a smaller slope than that of the shock trajectory. One may see how fast the region which shares less energy enlarges (area $?_c s_2 s_2$, Fig. 7) and how the initiation energy is mostly concentrated into the self-governing zone near the shock. This leads to a formation of a positive pressure gradient on the shock near $?_3$.

At the time γ_4 , $\theta=0$, the shock wave begins to accelerate which means the self-amplifying mechanism is dominant. At this point the form of the initial motion is forgotten completely. It is mainly due to the accumulated pressure energy just behind the shock. Forgetfulness of details of the initial conditions is also completed and selected memory may be represented by the shock properties, such as, pressure and Mach number at γ_{μ} (Figs. 10 and 12).

The increasing rate of the self-amplifying mechanism may be measured by the energy gradient on the shock but not by shock strength itself. Therefore, however the selected memories are different by initial conditions, the energy gradients are almost the same irrespective of the initial condition. It leads to the possibility of similarity motion later and forgetfulness in qualitative nature of the starting conditions.

Thus the coefficient A", total collapsing time $?_c$ will have direct relationships with the shock intensities at $?_4$ and the similarity index N will approach a constant irrespective of initiation energy since it relates to the energy gradient. The numerical results were shown in Table 1.

After 7_4 , the first positive density gradient at the shock front is always observed. This positive gradient spreads into a wider zone of the self-governing domain as time goes on. The kinetic energy contributes to self-amplification of the shock indirectly through rapid energy increase within the self-governing zone. One may see the continuous energy increase on the singularity line which is mainly due to this kinetic energy from 7_2 to 7_5 .

At the time $?_5$ the similarity domain finally starts. Here the singularity line and the limiting characteristic line join with the limiting similarity line. From $?_2$, both thermal and kinetic energies steadily increase on the limiting characteristic line and at time $?_5$ the energy densities at the shock and limiting characteristics are equal (Fig. 7).

Therefore, through energy interpretations, the similarity region may be characterized as starting when the flow within the self-governing domain has sufficient energy to keep the self-amplifying mechanism in operation.

4.4 Geometrical Effects

One can analyze the purely geometric effects into three parts;

namely, area convergence effects on the shock surface which leads to increasing the energy or pressure density on the shock wave, volumetric effect which leads to decreasing the mean energy density of the shocked gas in volume or mass and curvature effects.

If we assume that the shock surface keeps constant total initiation energy \mathbf{E}_{0} at every moment, then the shock surface energy density increases in the following manner:

$$E_{s.D.} = \frac{E_o}{s} / \frac{E_o}{S_o} = 1 / \left(\frac{R_s}{R_o}\right)^2$$
 (4.1)

where $E_0 = total$ initiation energy

 $S_o = initial surface at R_s = R_o$

S = instant shock surface at R_S = R_S

On the other hand, if we assume mean energy, density and pressure profiles in the shocked gas region, then the mean energy density will decrease in the following manner:

$$E_{ND.} = \frac{E_o}{V} / \frac{E_o}{V_o} = 1 / \left(1 - \left(\frac{R_s}{R_o}\right)^3\right) \tag{4.2}$$

where $V = \frac{4}{3} \pi R_s^3$

We call this a volumetric effect. Then the effects of these volumetric energy densities per shock surface can be written as:

$$E_{v.o.s.} = 3E_{v.o.} = 3/(1-(\frac{R_s}{R_o})^3)$$
 (4.3)

We call this a volumetric effect per area.

The variations of those three effects with respect to shock radius are plotted in Fig. 17. We can see how the volumetric effects are stronger than area convergence effects at the early stage. Therefore, the shock initially decelerates very fast as the initiation energy is being distributed over an increasing mass of gas engulfed by the shock.

The assumption of constant energy density at the shock may be applied for the case of infinite initiation energy, i.e. $c_j^{*2} = 0$. Since the volumetric effect per area decelerates the shock wave, but the area effect accelerates it, the intersection of these two curves may give the point where shock acceleration is zero, i.e. $\theta = 0$. From Fig. 17 we have $R_s/R_o = 0.53$ for this point, and the result coincides surprisingly well with the numerical result (Table 1).

Since pressure is area phenomena, both area effects and volumetric effects per area can be applied for the pressure immediately behind
the shock as well as the energy density at the shock front. Thus,
another characteristic point where the area effect and the relative
volumetric effect per area with respect to pressure are equal in magni-

tudes can be found. This point may give the location where the pressure gradient at the shock front becomes zero. Graphical estimation of Fig. 17 gives $R_{\rm S}/R_{\rm O}=0.665$ for this point, and one may see close agreement with the numerical result (Fig. 9) where the positive pressure gradient was first observed.

From this simple analysis one may see how the motion of a converging shock wave is strongly affected by purely geometrical effects.

REFERENCES

Akinsete, A.

"Hydrodynamics of a Spherical Cavity Collapsing in a Liquid" McGill University Gasdynamics Lab. Report 68-1, 1968.

Bach, G. G. and Lee, J. H.

"Initial Propagation of Impulsively Generated Converging Cylindrical and Spherical Shock Waves" Paper presented at the Canadian Congress of Applied Mechanics held at Laval University, Quebec, Canada, May 1967. (To be published in The Journal of Fluid Mechanics.)

Butler, D. S.

"Converging Spherical and Cylindrical Shocks"

ARE Report 54/54, December 1954.

Chester, W.

"The Quast-Cylindrical Shock Tube" Phil. Mag. 45, 1293, 1954.

Chisnell, R. F.

"The Normal Motion of a Shock Wave through a Normalform One-Dimensional Medium"

Proc. Roy. Soc. A232, 350, 1955.

Chisnell, R. F.

"The Motion of a Shock Wave in a Channel, with Applications to Cylindrical and Spherical Shock Waves"

J. Fluid Mech. 2, 286, 1957.

Chou, P. C. and Karpp, R. R.

"Solution of Blast Wave by the Method of Characteristics"
DIT Rep. No. 125-7, 1965.

Chou, P. C. and Burns, B. P.

"Late-Stage Equivalence in One-Dimensional Impacts"

J. Appl. Phy., Vol. 38, No. 2, 1967.

Courant, R. and Friedrichs, K. O.

"Supersonic Flow and Shock Waves" Interscience Publishers, New York, 1948.

Guderley, G.

"Powerful Spherical and Cylindrical Compression Shocks in the Neighbourhood of the Center of the Sphere and of the Cylinder Axis"

<u>Luftfahrtforschung</u>, Vol. 19, No. 9, October 1942.

Hartree, D. R.

"Numerical Analysis"
Oxford University Press, 1958.

Ho, D. V., Shen, M. C. and Meyer, R. E. "Climb of a Bore on a Beach", Parts 1, 2 and 3

J. Fluid Mech. 14, 15, 16, 1962.

Huang, S. L. and Chou, P. C.

"Solution of Blast Waves by a Constant Time Scheme in the Method of Characteristics" DIT Rep. No. 125-9, 1966.

Huang, S. L. and Chou, P. C.

"Calculations of Expanding Shock Waves and Late-Stage Equivalence" DIT Rep. No. 125-12, 1968.

Hun	ter	. C	

"On the Collapse of an Empty Cavity in Water"

J. Fluid Mech. 7, 4, 1960.

Keller, H. B., Levine, D. A. and Whitham, G. B. "Motion of a Bore on a Sloping Beach"

J. Fluid Mech. 7, 302, 1960.

Lax, P. D.

"Weak Solutions of Non-Linear Hyperbolic Equations and Their Numerical Computations"

Comm. Pure Appl. Math. 7, 1954.

Lax, P. and Wendroff, B.

"Systems of Conservation Laws"

Comm. Pure Appl. Math. 8, 1960.

Lax, P. D. and Wendroff, B.

"On the Stability of Difference Schemes"

Comm. Pure Appl. Math., 15, 1962.

Lee, B. H. K.

"Non-Similar Solutions of Imploding Shocks and Detonations" McGill University Gasdynamics Lab., Report 66-1, 1966.

Payne, R. B.

"A Numerical Method for a Converging Cylindrical Shock"

J. Fluid Mech. 2, 185, 1957.

Richtmyer, R. D. and Morton, K. W.

"Stability Studies for Difference Equations"
NYO-1480-5, 1964.

Stanyukovich, K. P.

"Unsteady Motion of Continuous Medium"

Pergamon Press, 1960.

Welsh, R. L.

"Imploding Shocks and Detonations"
University of California, College of
Engineering, Rep. No. AS-66-1, 1966.

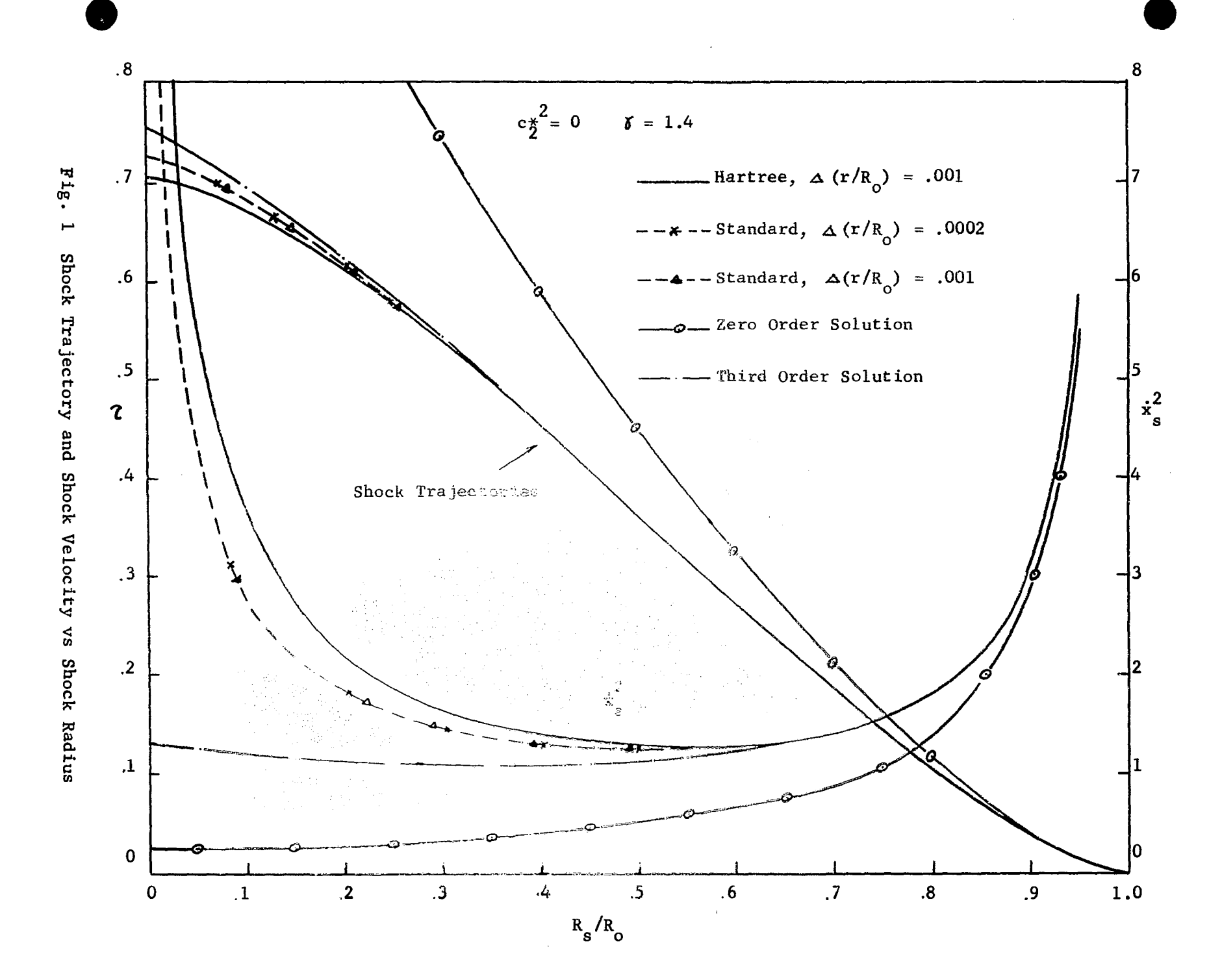
Whitham, G. B.

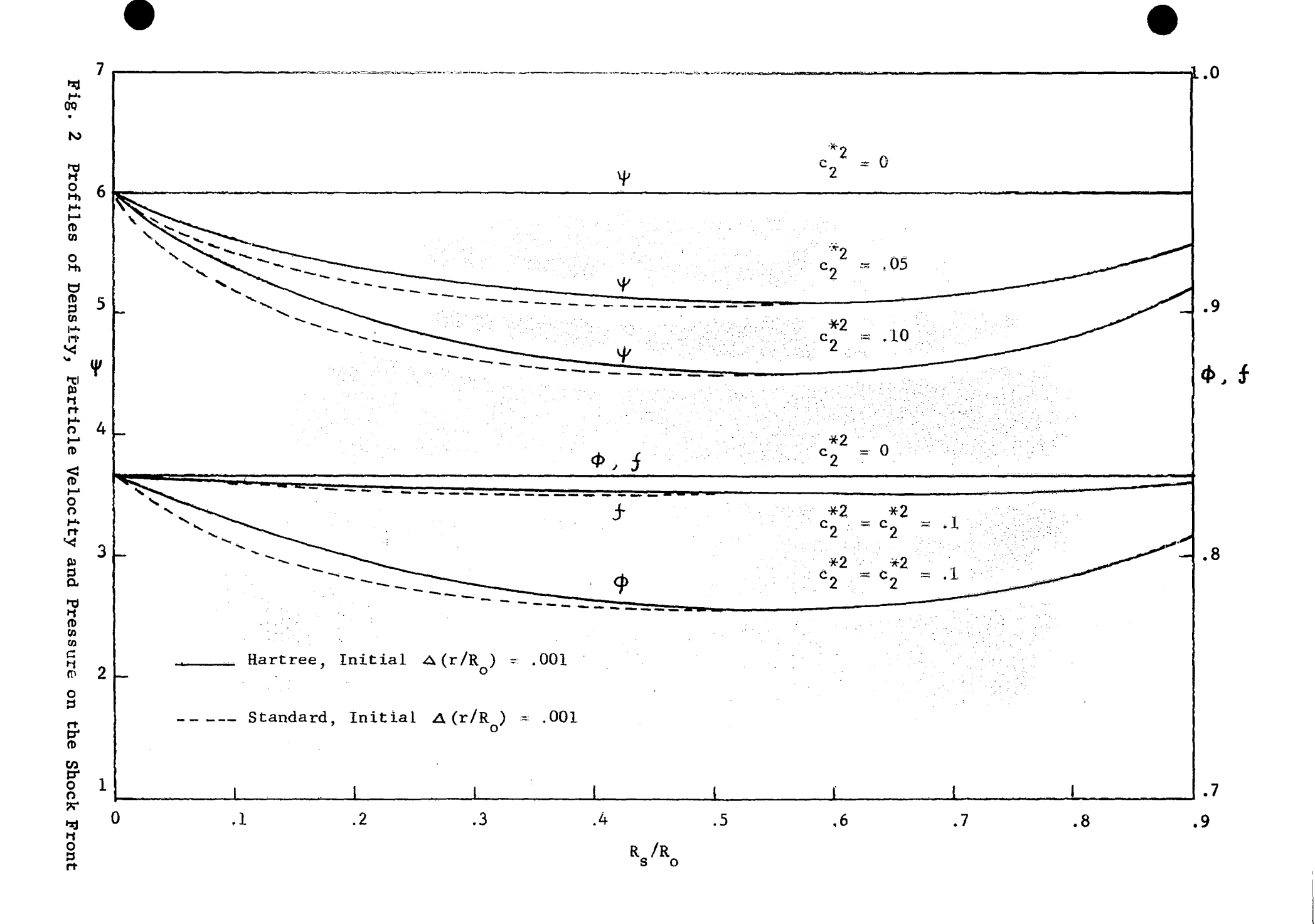
"On the Propagation of Shock Waves through Regions of Non-Uniform Area of Flow"

J. Fluid Mech. 4, 337, 1958.

Zeldovich, Ya. B.

"Physics of Shock Waves and High-Temperature Hydrodynamic Phenomena" U. S. A. Force, Patterson Base, Tech. Trans. FTD-MT-64-514, 1960.





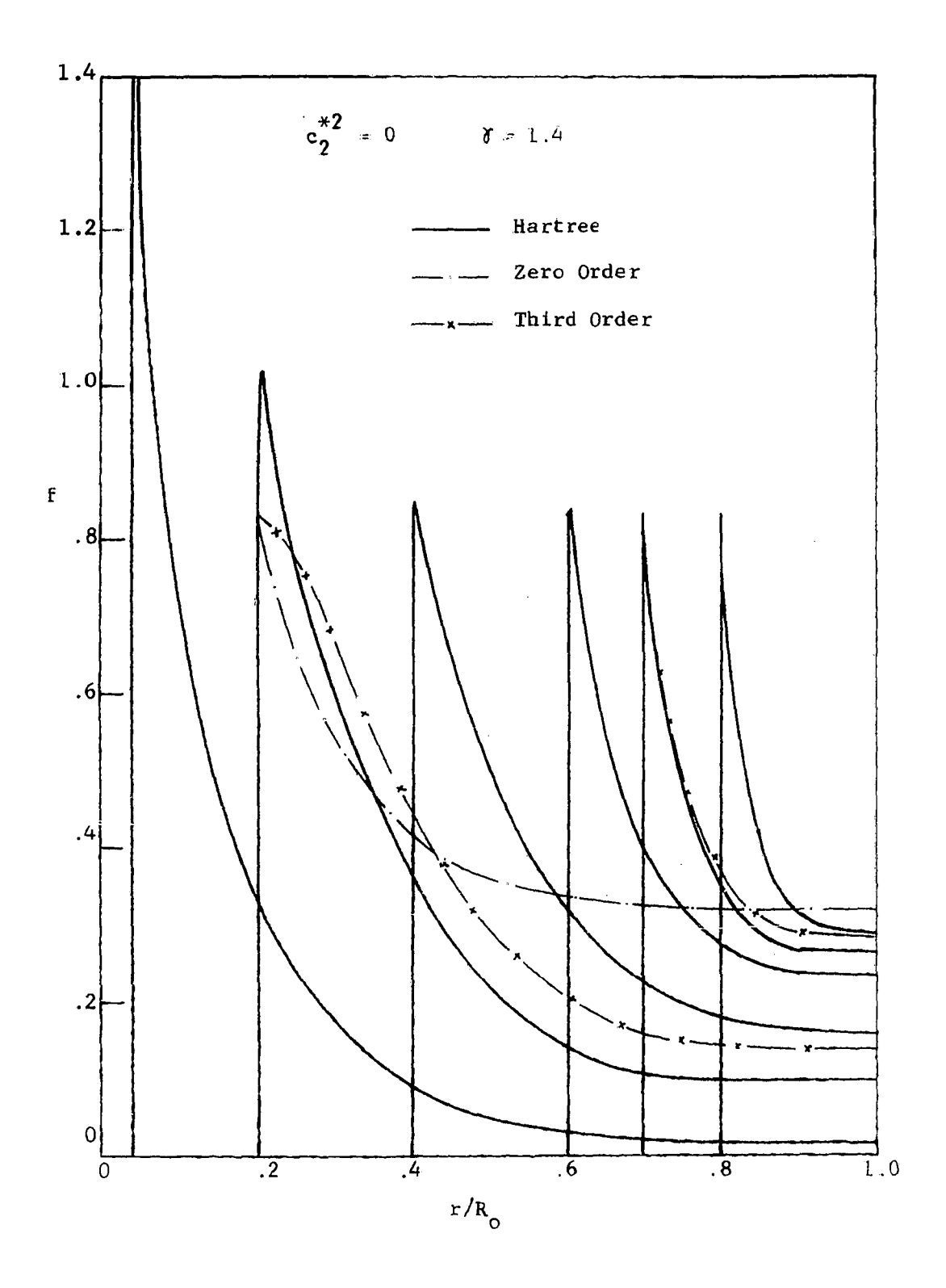


Fig. 3 Pressure Profiles

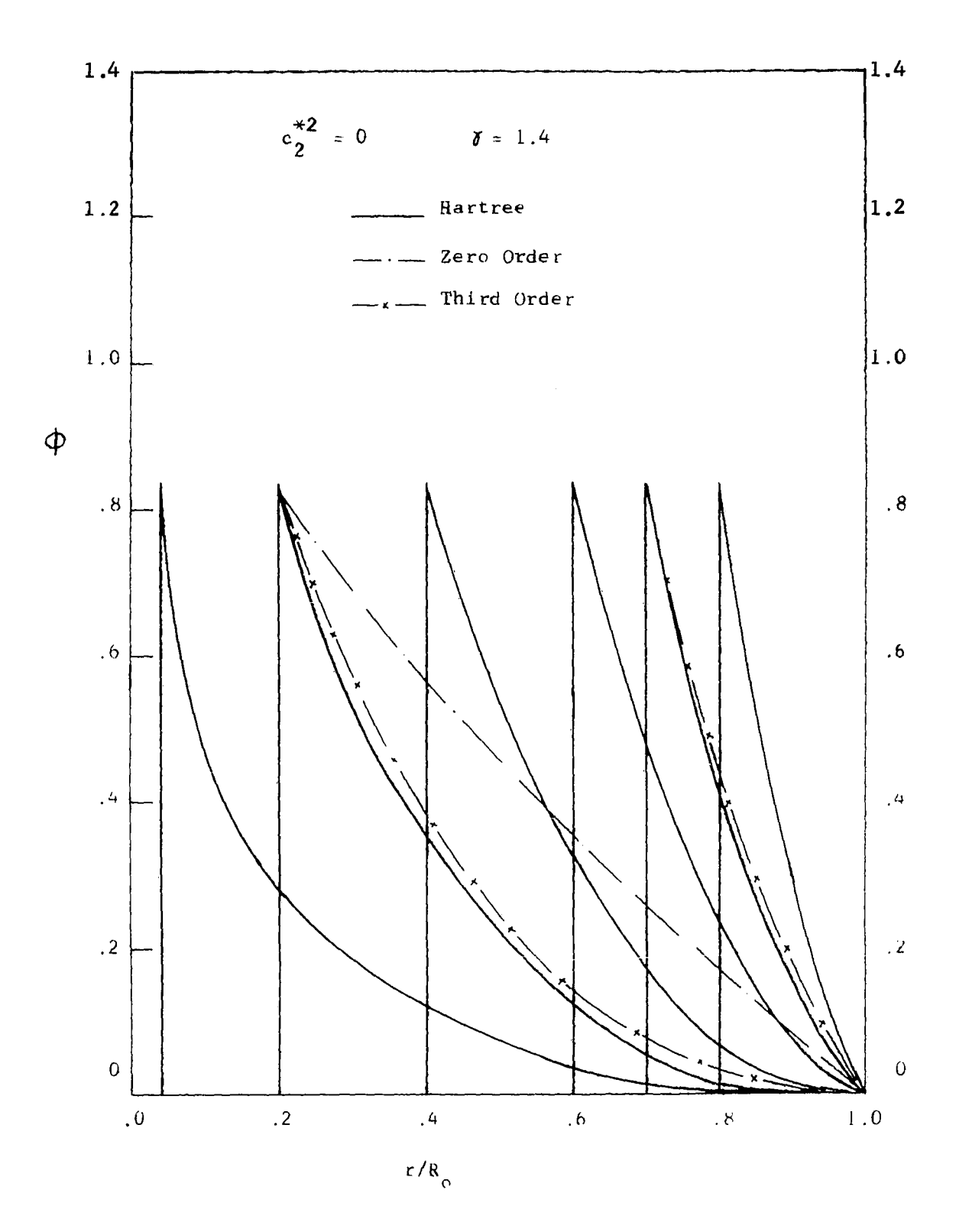


Fig. 4 Particle Velocity Profiles

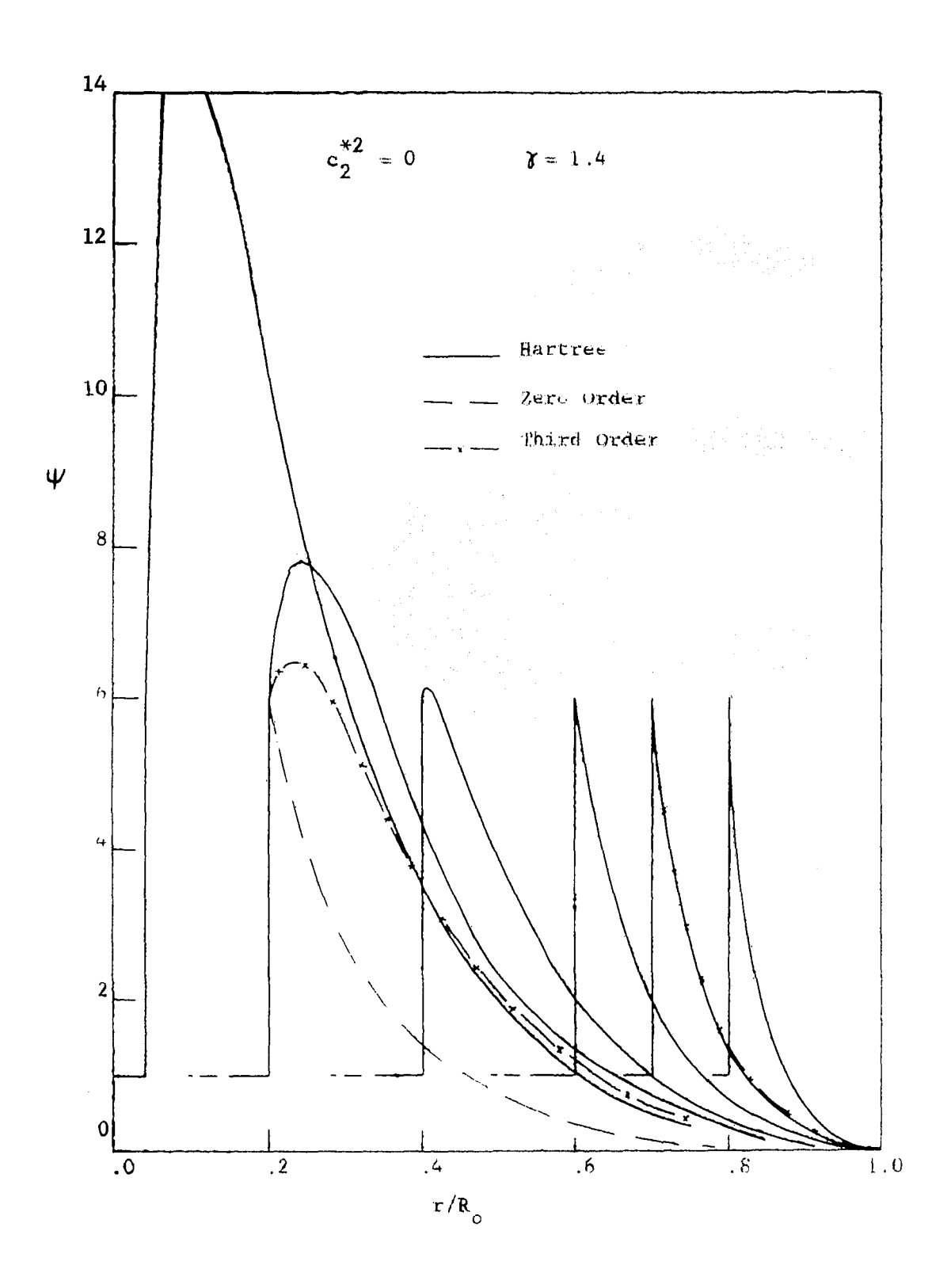


Fig. 5 Density Profiles

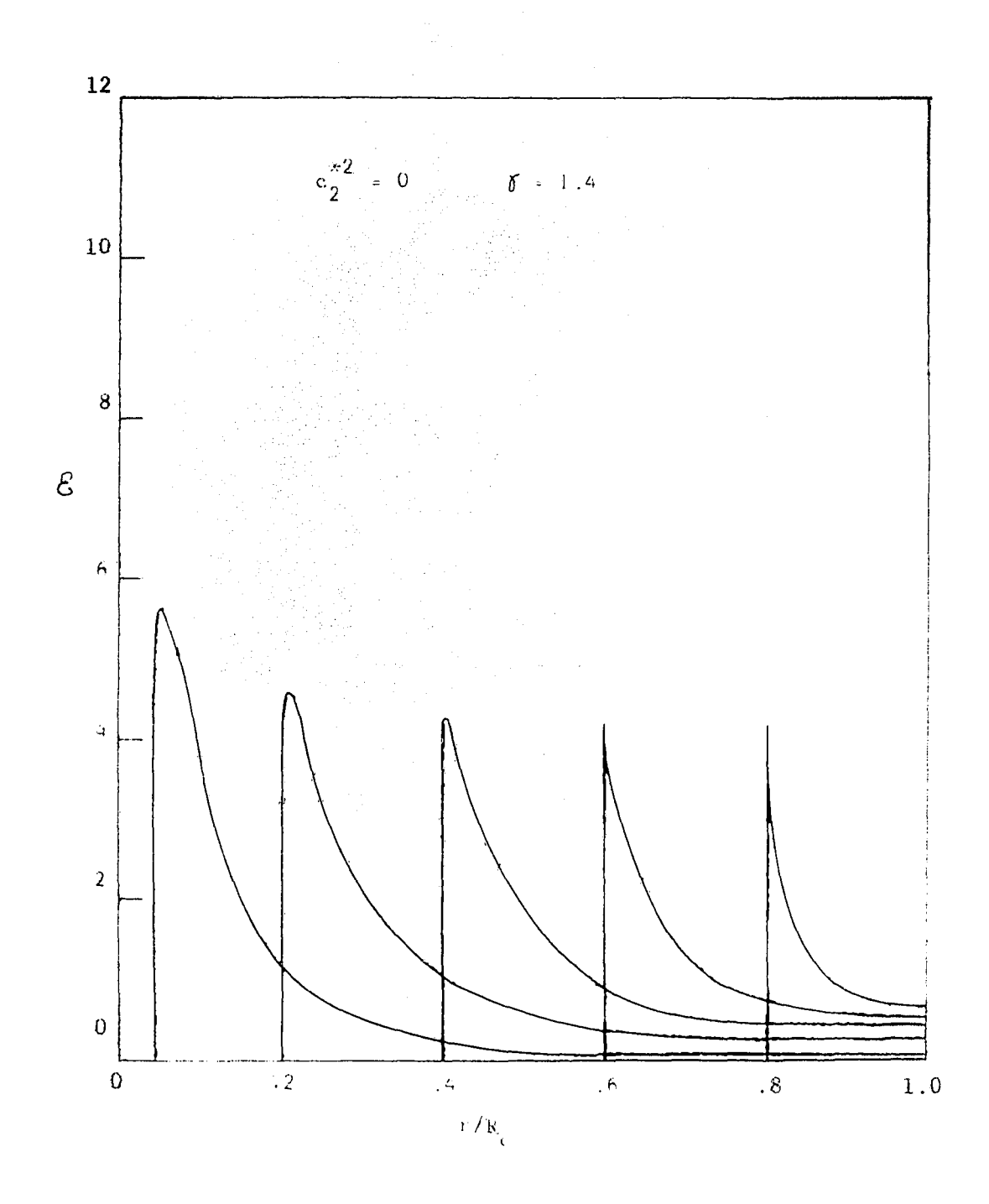
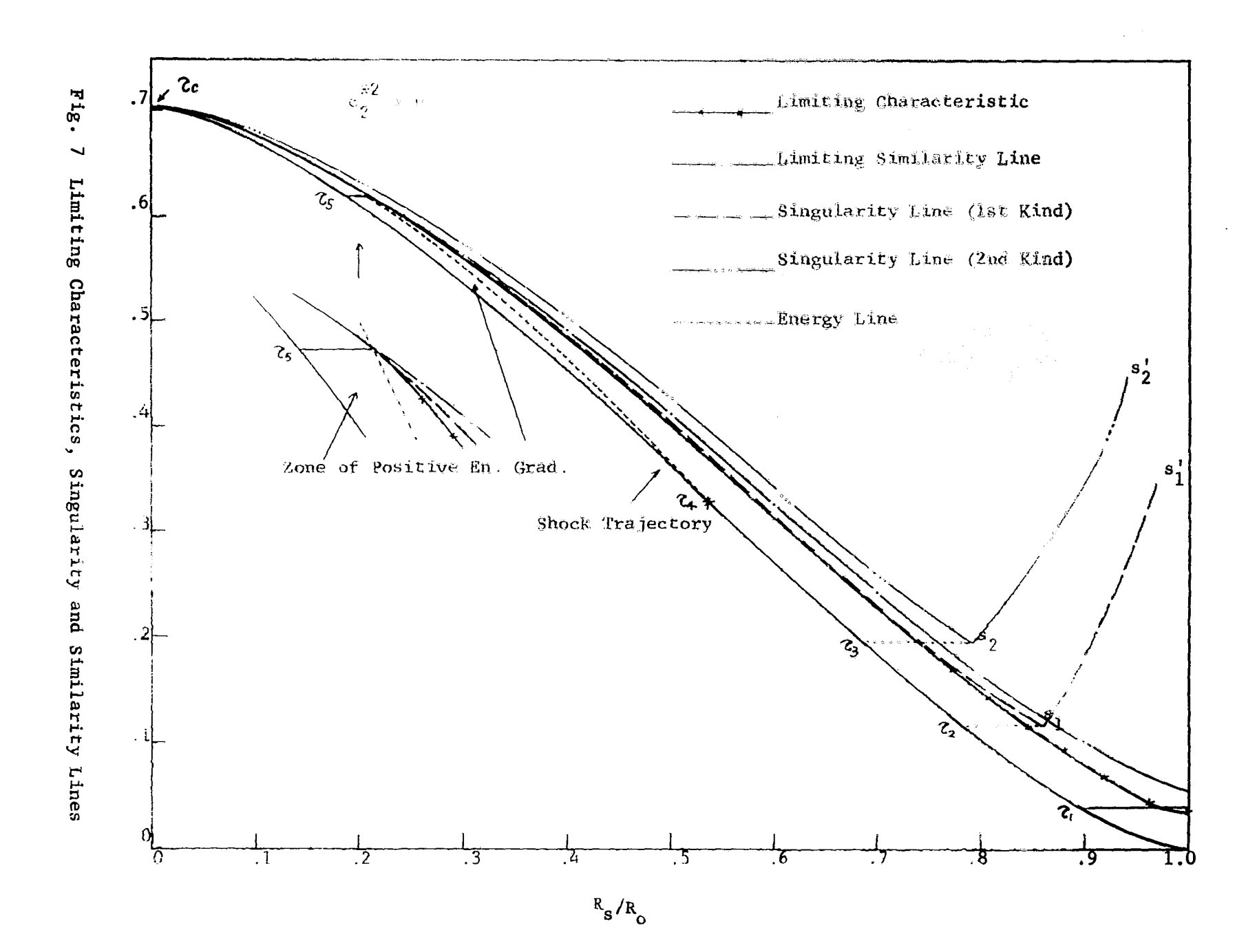
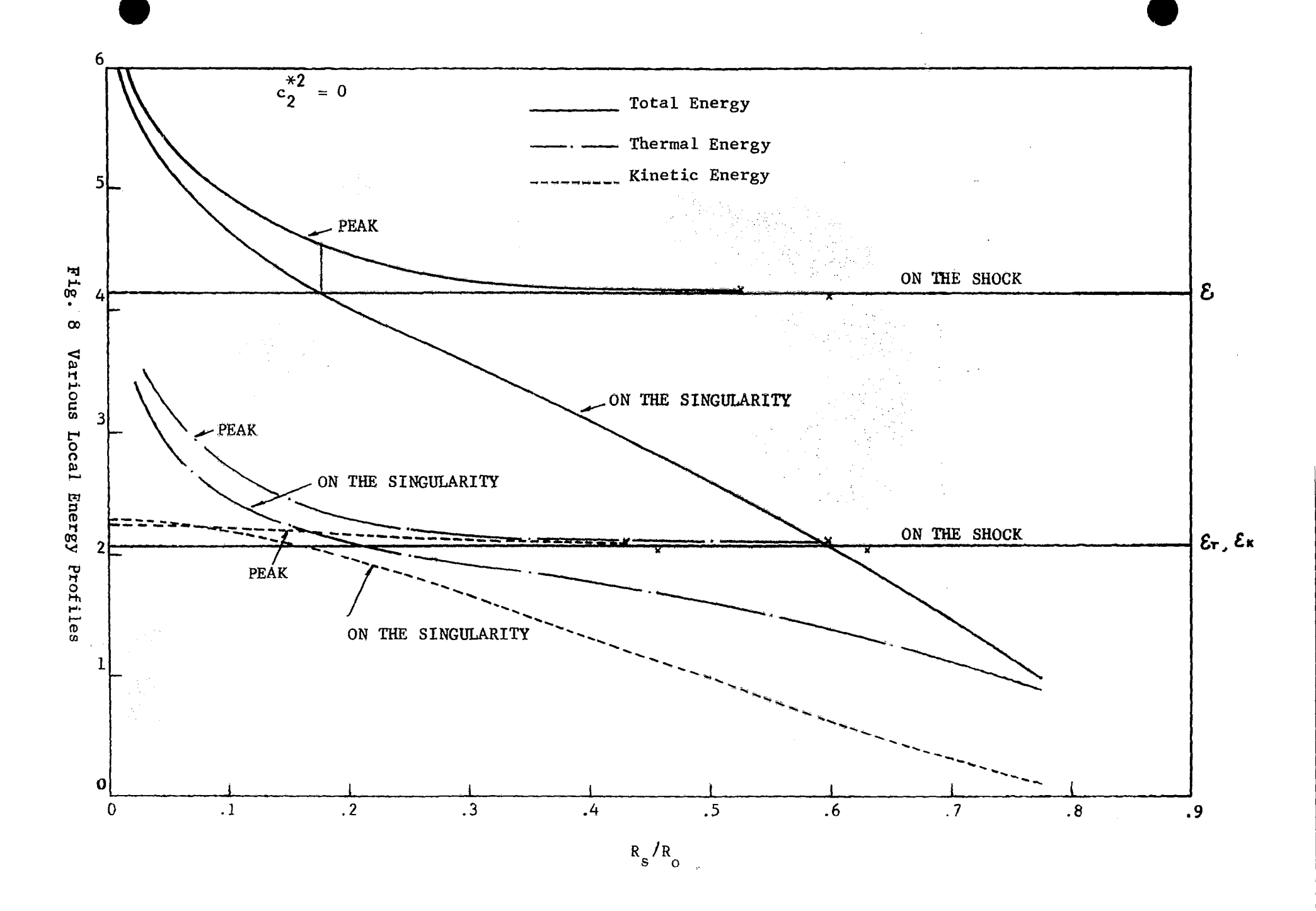


Fig. 6 Local Energy Distributions





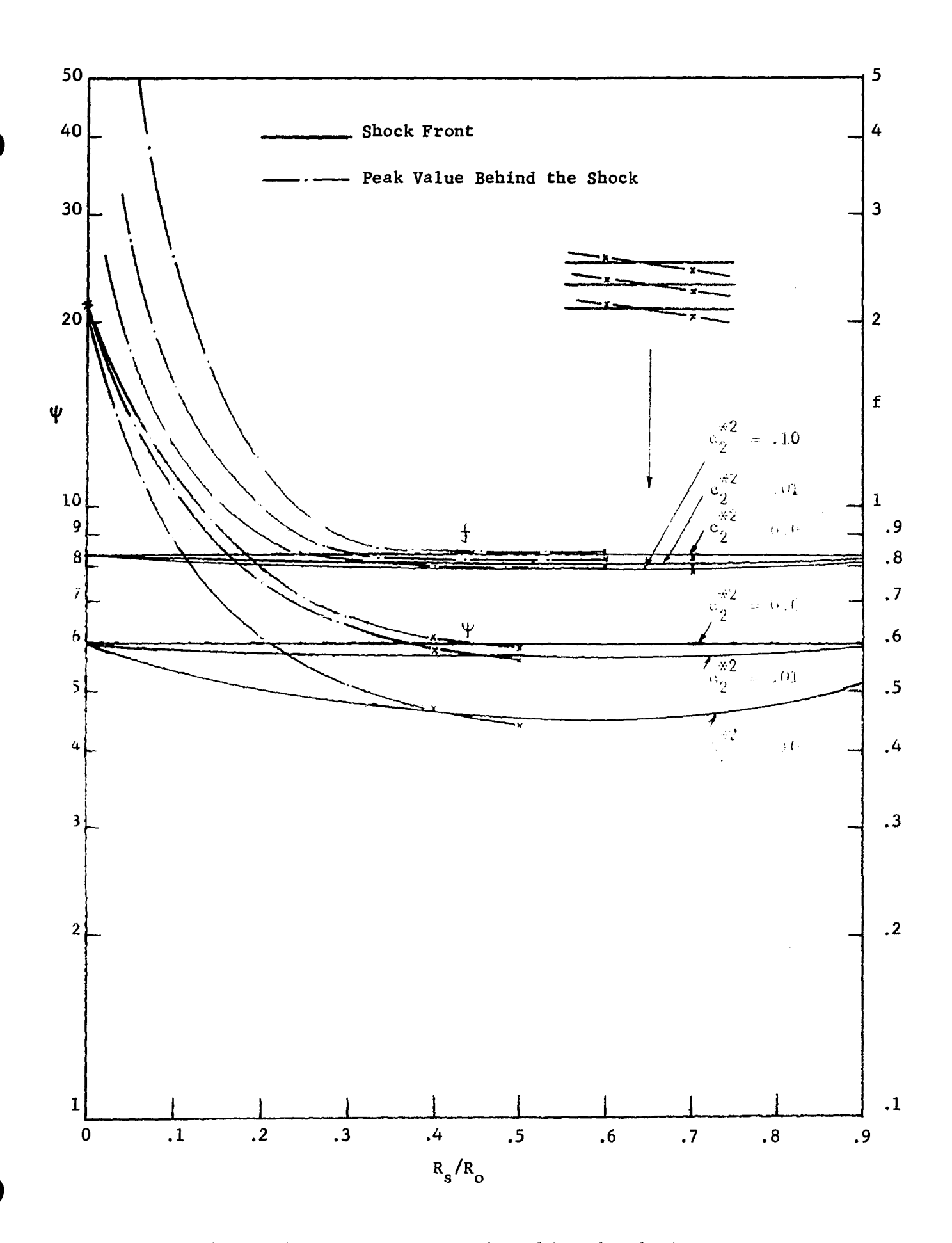
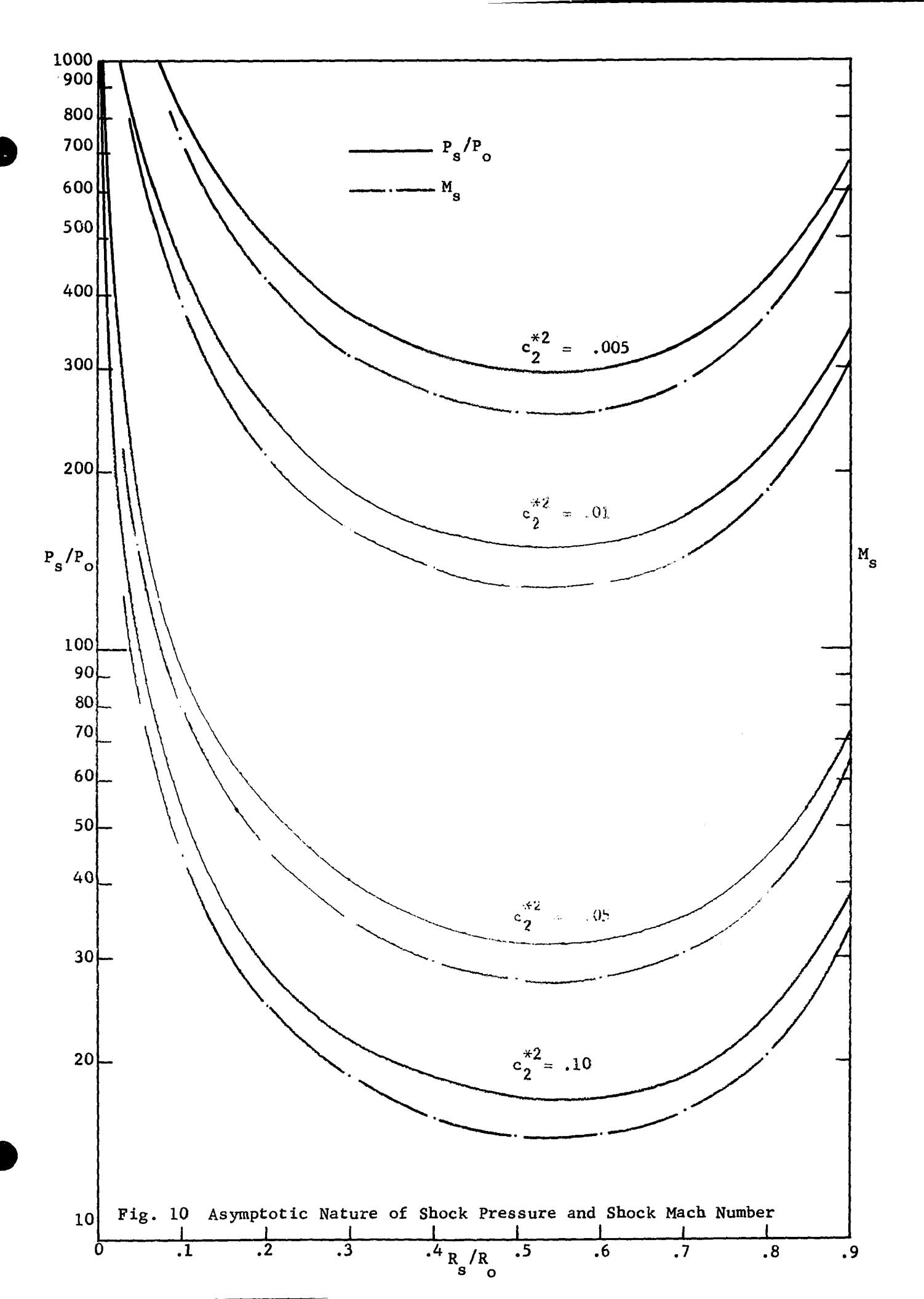
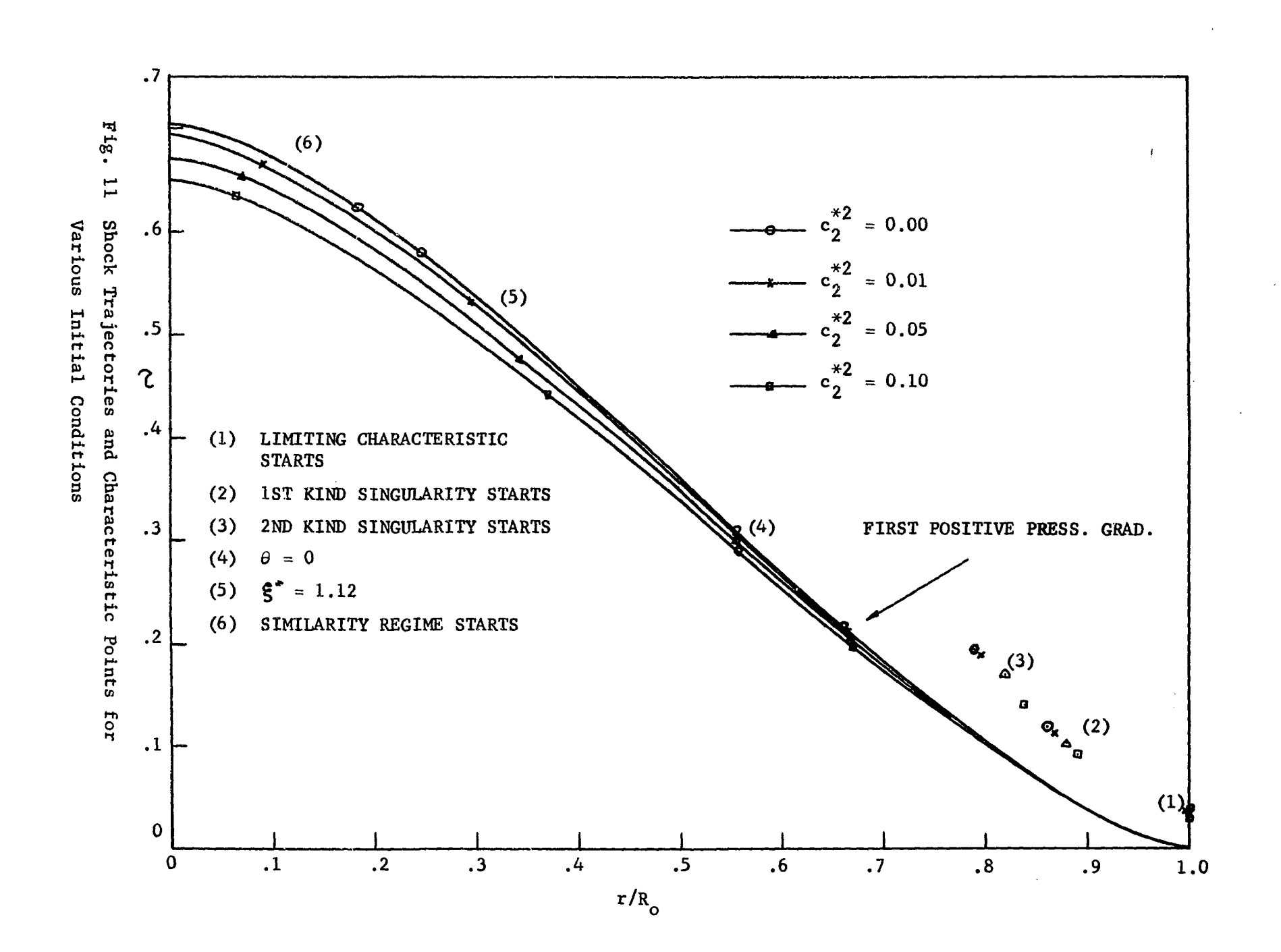
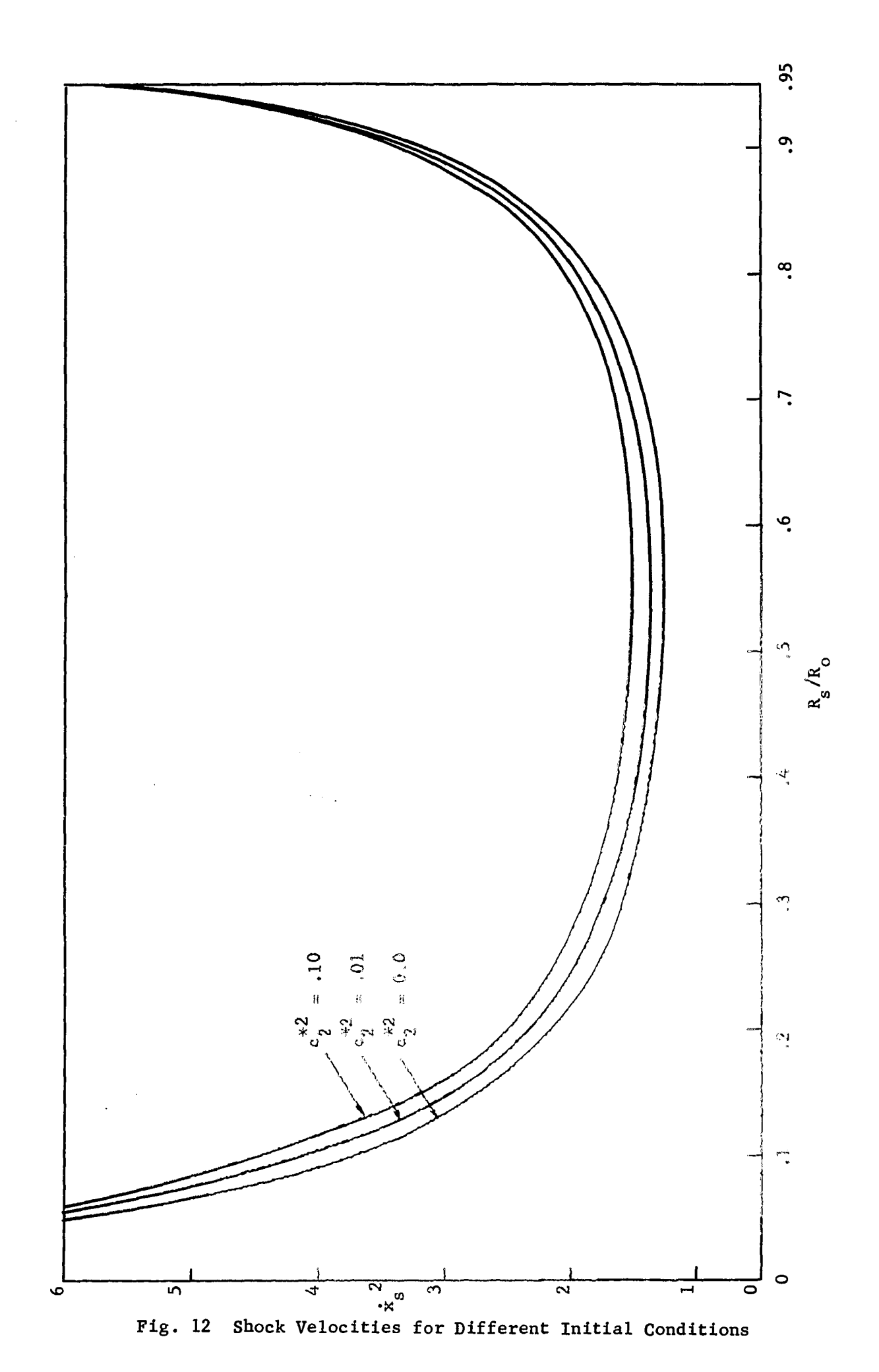


Fig. 9 Density and Pressure Peaks Behind the Shock Front







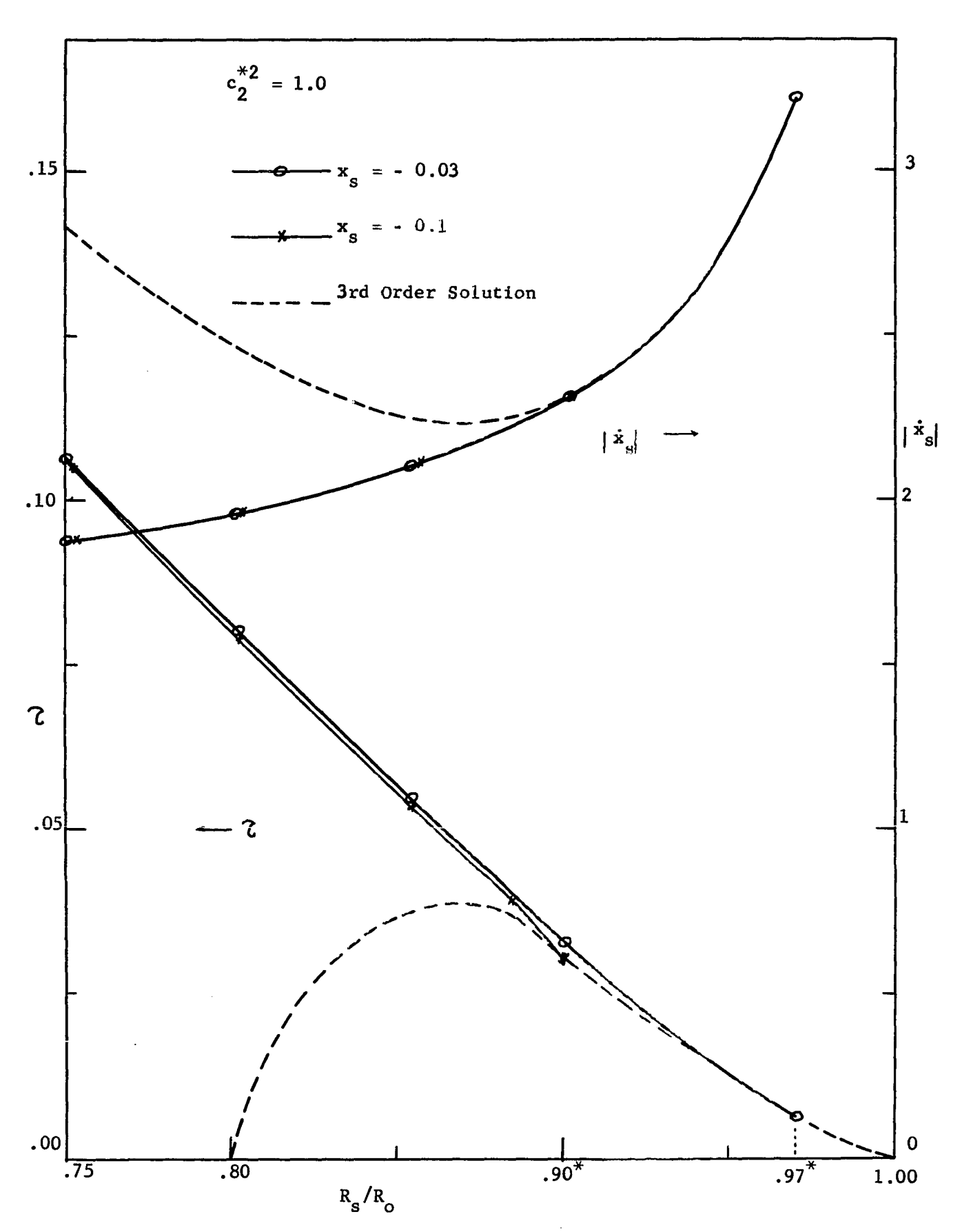


Fig. 13 Shock Trajectory and Wave Velocity for Different Starting Time Lines

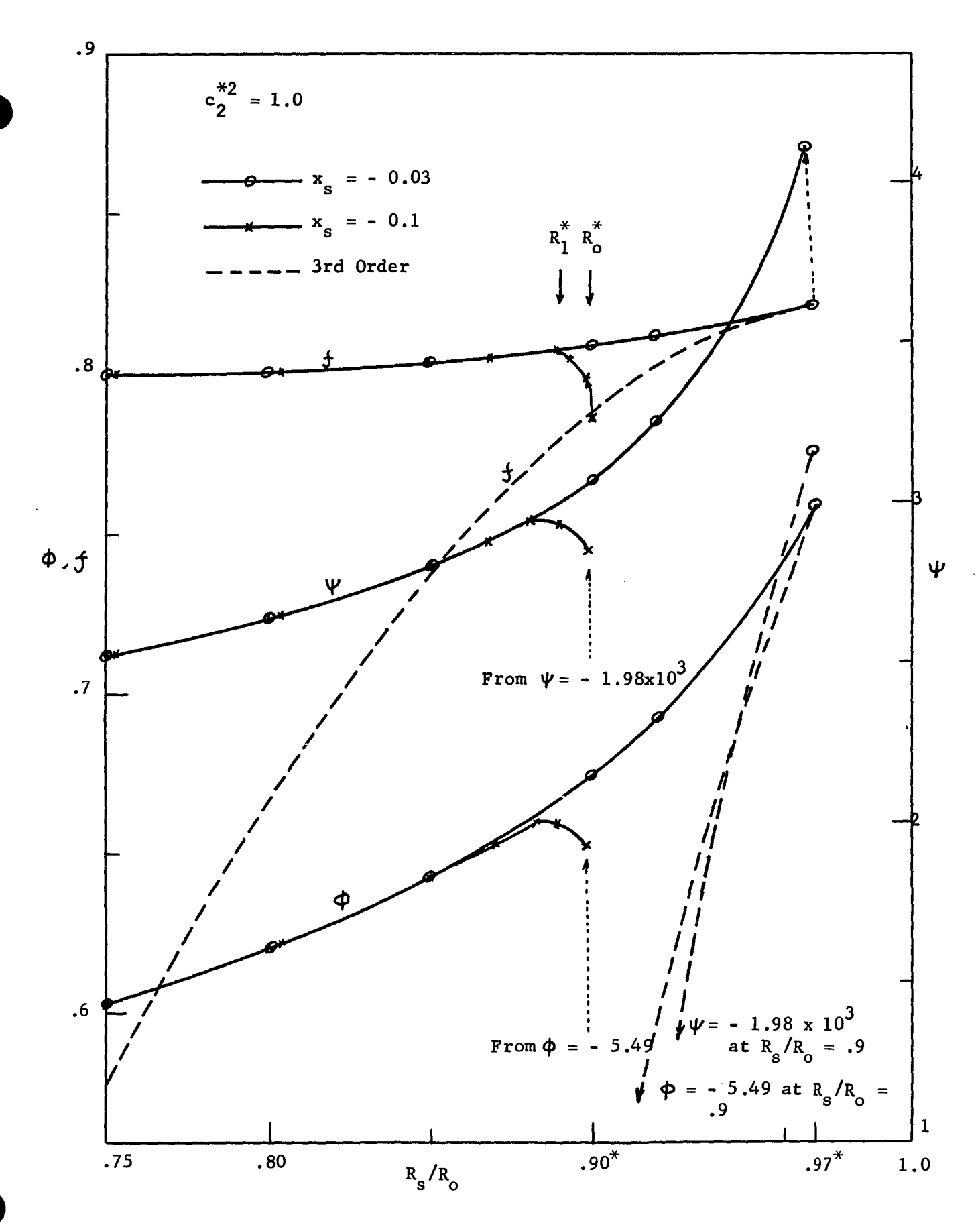


Fig. 14 Density, Pressure and Particle Vel. Profiles on the Shock Wave for Different Starting Time Lines

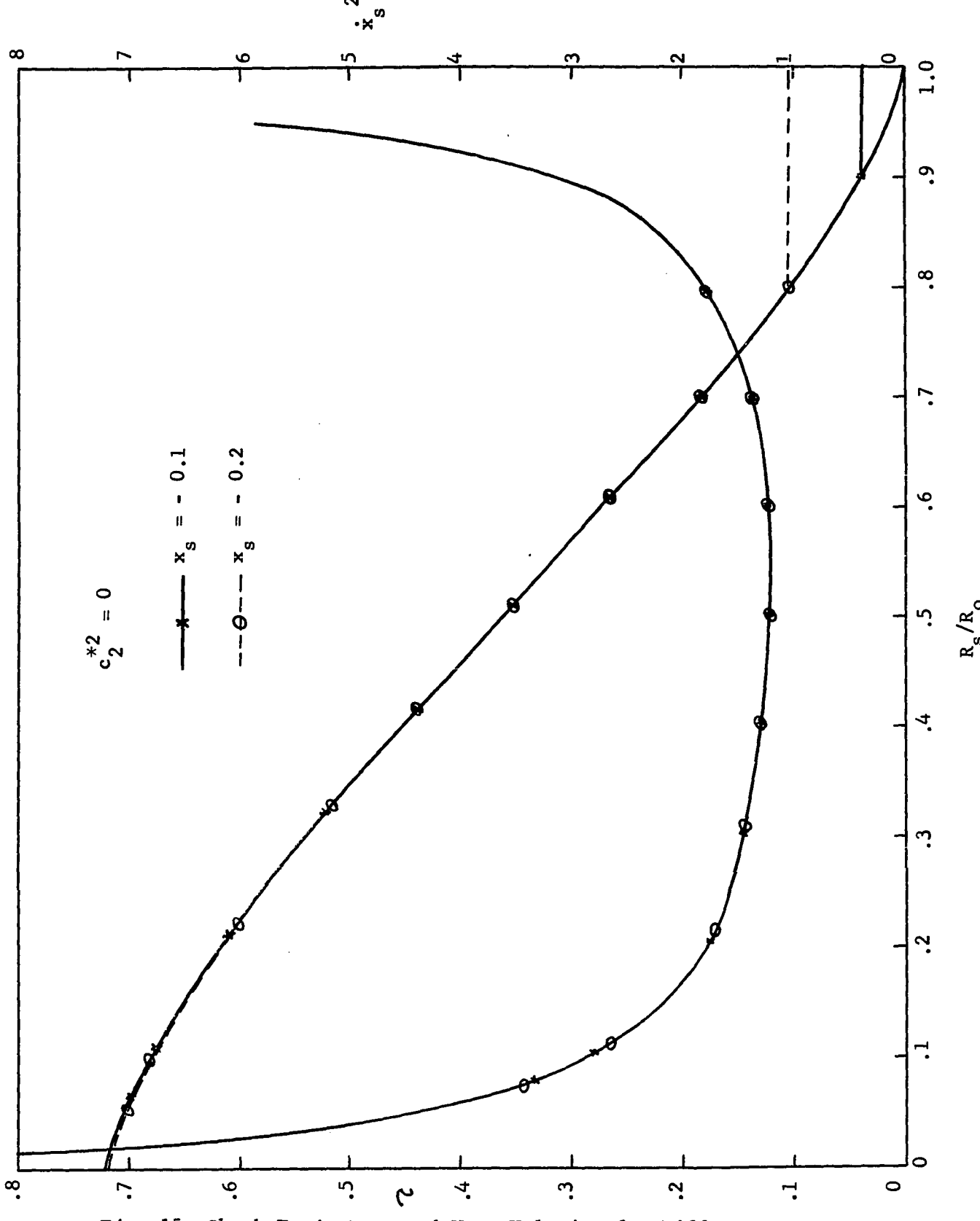
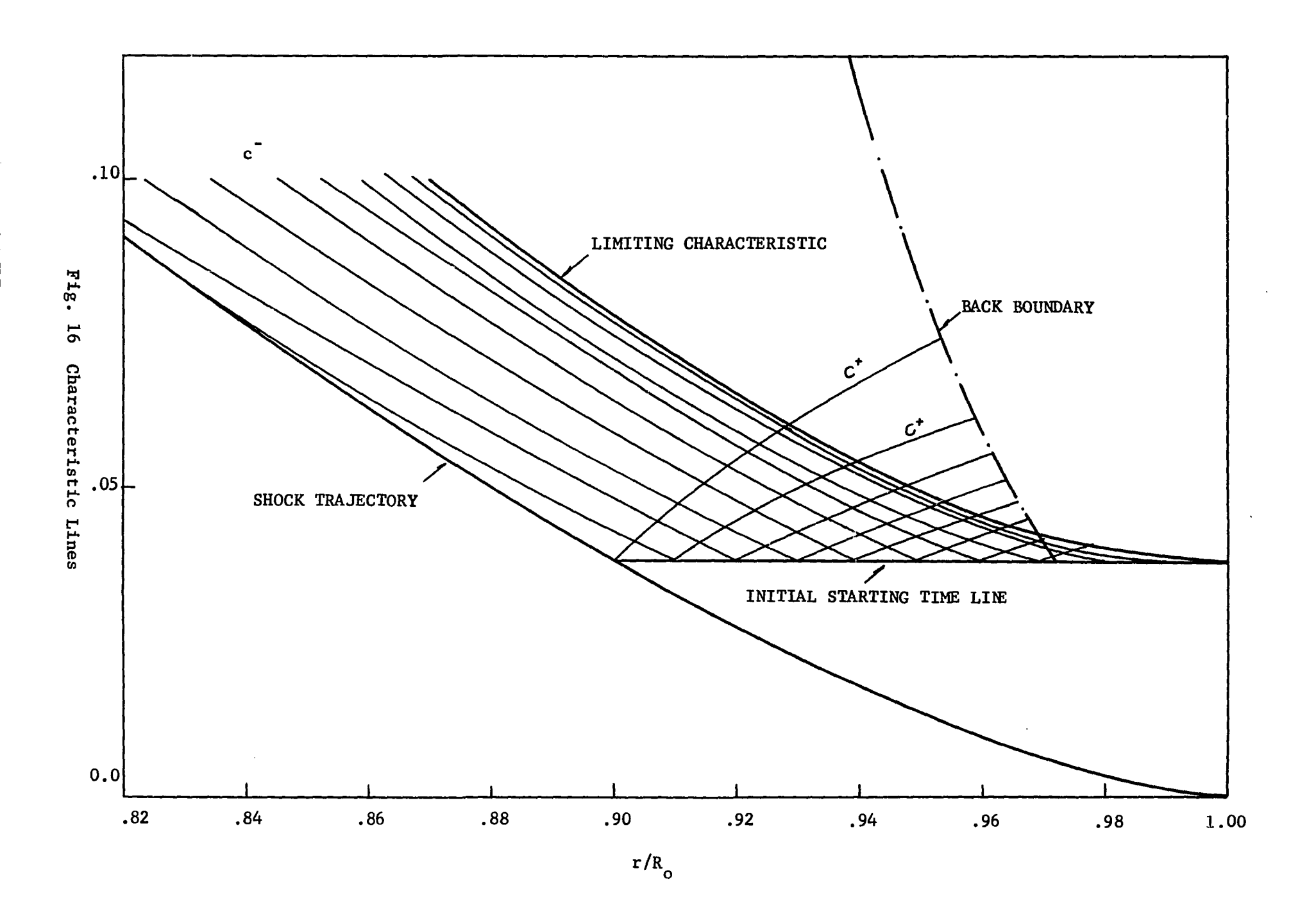
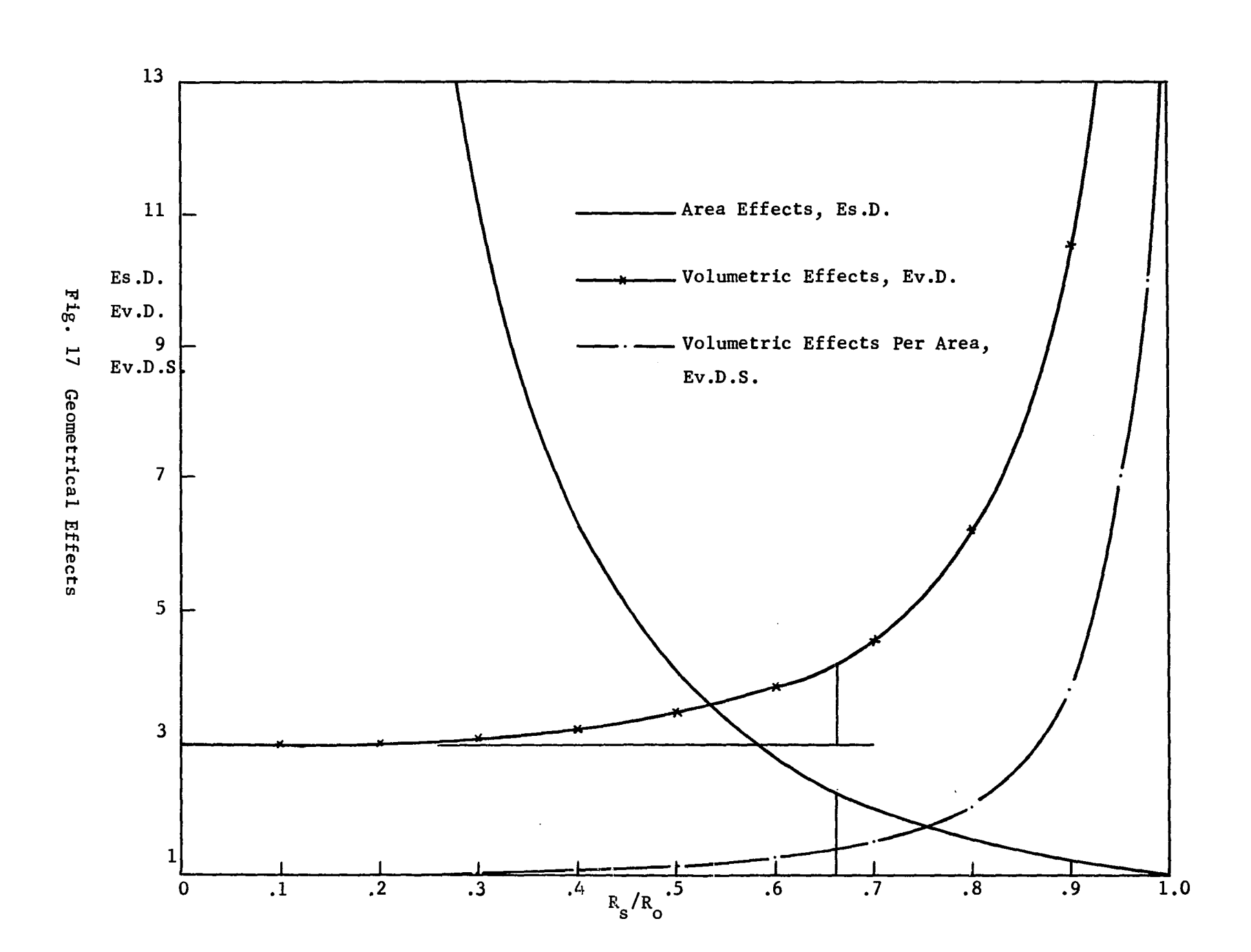


Fig. 15 Shock Trajectory and Wave Velocity for Different Starting Time Lines (Standard Scheme)





c*2 j	Α'	t'c	Α"	℃.	N	M _s ²	(R _s /R _o)*
0.0	œ	0.00	1.06585	0.705375	0.717173	œ	0.184968
0.005	7.13818	0.0496017	1.06780	0.701535	0.717166	481.236	0.174950
0.010	5.56004	0.0698226	1.06825	0.698226	0.716386	443.516	0.083869

$$R_{s}/R_{o} = A'(t'_{c} - t')^{N}, t' = tC_{o}/R_{o}$$
 $R_{s}/R_{o} = A''(?_{c} - ?)^{N}$

 $(R_s/R_o)^*$: The point where similarity solution starts.

TABLE 1

VARIATION OF N WITH c_j^{*2} FOR SPHERICAL SHOCK WAVES ($\delta = 1.4$)